

ELECTROCHEMICAL INVESTIGATION OF CARBON DIOXIDE CORROSION OF
MILD STEEL IN THE PRESENCE OF ACETIC ACID

A thesis presented to
the faculty of
the Fritz. J. and Dolores H. Russ College of Engineering and Technology of
Ohio University

In partial fulfillment
of the requirements for the degree

Master of Science

Keith S. George

March 2003

This thesis entitled
ELECTROCHEMICAL INVESTIGATION OF CARBON DIOXIDE CORROSION OF
MILD STEEL IN THE PRESENCE OF ACETIC ACID

by
Keith S. George

has been approved for
the Department of Chemical Engineering
and the Russ College of Engineering and Technology by

Srdjan Nesic
Professor of Chemical Engineering

Dennis Irwin
Dean, Russ College of Engineering and Technology

GEORGE, KEITH S. M.S. March 2003. Chemical Engineering

Electrochemical Investigation of Carbon Dioxide Corrosion of Mild Steel in the Presence of Acetic Acid (p 90)

Director of thesis: Srdjan Nestic

The corrosion behavior of mild steel in the presence of acetic acid and carbon dioxide has been investigated using electrochemical techniques and weight loss (WL) measurements. Acetic acid (HAc) was found to retard the anodic reaction (iron dissolution) and act as an additional source of hydrogen ions, which increased the measured limiting currents. The corrosion rate of carbon steel in the presence of HAc was found to be under charge transfer control and the mechanism for both the cathodic and anodic reactions remained the same. The possibility of direct reduction of HAc was not supported from the experimental results and electrochemical modeling.

A series of experiments was also performed to study the effect of calcium ions and simulated brines on the corrosion rate of mild steel in the presence of acetic acid. The corrosion rates of mild steel were found to be similar in simulated brines and sodium chloride solutions. Increasing amounts of calcium ions was found to decrease the corrosion rate of mild steel. However, when acetic acid is present, the corrosion rate still remains at a high value.

A wide range of HAc concentrations (0-5000 ppm), temperatures (22-80°C), pHs (4-6) and rotational velocities (500-4000 rpm) was used to develop an electrochemical model to predict the experimental data. The cathodic limiting currents were not found to result from a chemical reaction limitation but rather a mass transfer one. The model and the experimental potentiodynamic sweeps are in very good agreement at low

temperatures. Thus, the predicted corrosion rates are in very good agreement with LPR and WL measurements at low temperatures.

A modification to the de Waard (1995) model was made to account for the presence of HAc. The de Waard model, with the modification, agrees well with the experimental data at temperatures of 40°C and above. At low temperatures, the de Waard model is not in agreement with the experimental data and is too conservative in the prediction of the corrosion rate.

Approved: Srdjan Nesic
Professor of Chemical Engineering

ACKNOWLEDGMENTS

The author would like to thank his advisor, Dr. Srdjan Nestic, for the advice and mentoring throughout the experimental program.

The author would also like to thank the technical staff at the Institute for Corrosion for their expertise in designing and building laboratory equipment. The support of Dr. Charles Alexander, Interim Director of the Institute for Corrosion should also be mentioned. Dr. Alexander's guidance during a very critical time in the history of the Institute is greatly appreciated.

Last and not least, the author thanks the students of the Institute for their advice and support throughout the project. The author would like to give special mention to Bruce Brown, Yuhua Sun and Frederic Vitse.

Table of Contents

1. Introduction.....	11
1.1. CO ₂ Corrosion	12
1.2. Acetic Acid Corrosion	14
1.3. Rotating Cylinders	17
2. Test Matrix and Research Objectives	19
3. Experimental Setup.....	21
3.1. Potentiodynamic Sweeps	23
3.2. Weight Loss Experiments.....	24
4. Results and Discussion	25
4.1. Water Chemistry Calculations.....	25
4.2. The Effect of HAc In Solutions De-Oxygenated Using N ₂ and CO ₂	27
4.3. The Effect of HAc Concentration in the Presence of Carbon Dioxide.....	32
4.4. The Effect of pH	37
4.5. The Effect of Rotational Velocity.....	38
4.6. The Effect of Temperature.....	39
4.7. Repeatability of Potentiodynamic Sweeps	40
4.8. Weight Loss Experiments.....	42
4.9. The Effect of Ca ²⁺	45
4.10. The Effect of Simulated Brines	49
5. Electrochemical Modeling	51
5.1. Hydrogen Reduction	51
5.2. Limiting Current From HAc	54
5.3. Limiting Currents Arising From the Presence of CO ₂	59
5.4. Water Reduction	60
5.5. The Anodic Dissolution of Iron	60
5.6. Implementation of the Model	61
6. Semi-Empirical Corrosion Modeling.....	62
6.1. The de Waard Corrosion Model (1995).....	62
6.2. An Extension of the de Waard Model to Account for the Presence of HAc	65
7. Comparison Between the Electrochemical Model and Experimental Data.....	67
7.1. Anodic Reaction	67
7.2. The Effect of HAc In Solutions De-Oxygenated Using CO ₂	68
7.3. The Effect of HAc In Solutions De-Oxygenated Using N ₂	72
7.4. The Effect of Rotational Velocity.....	74
7.5. The Effect of pH	77
7.6. The Effect of Temperature.....	79
8. Comparison Between the Models and Experimental Data	82
9. Conclusions and Future Work	86
9.1. Conclusions.....	86
9.2. Future Work.....	87
10. References.....	88

List of Figures

Figure 1. Schematic of the test cell.	22
Figure 2. The effect of pH on the concentration of species at 1 bar CO ₂ , 22°C and 10 ppm HAc added.	26
Figure 3. The effect of pH on the concentration of species at 1 bar CO ₂ , 22°C and 100 ppm HAc added.	26
Figure 4. The concentration of undissociated HAc as a function of concentration added and system pH at 22°C.	27
Figure 5. Potentiodynamic sweeps in bubbling N ₂ solutions containing 0, 100, and 1000 ppm HAc (pH 4, 1000 rpm, 22°C).	29
Figure 6. The effect of HAc concentration on the corrosion rate of X-65 steel in bubbling N ₂ solutions (pH 4, 1000 rpm, 22°C).	29
Figure 7. Comparison between potentiodynamic sweeps in bubbling CO ₂ and N ₂ solutions containing 0 ppm HAc (pH 4, 1000 rpm, 22°C).	30
Figure 8. Comparison between potentiodynamic sweeps in bubbling CO ₂ and N ₂ solutions containing 100 ppm HAc (pH 4, 1000 rpm, 22°C).	31
Figure 9. Comparison between potentiodynamic sweeps in bubbling CO ₂ and N ₂ solutions containing 1000 ppm HAc (pH 4, 1000 rpm, 22°C).	31
Figure 10. The effect of HAc concentration on the cathodic potentiodynamic sweeps in bubbling CO ₂ solutions (0 – 5000 ppm HAc, pH 4, 1000 rpm, 22°C).	33
Figure 11. The effect of HAc concentration on the anodic potentiodynamic sweeps in bubbling CO ₂ solutions (0 – 5000 ppm HAc, pH 4, 1000 rpm, 22°C).	33
Figure 12. The effect of HAc concentration on the Nyquist impedance plots in bubbling CO ₂ solutions. (0, 100 ppm HAc, pH 4, 1000 rpm, 22°C).	34
Figure 13. The effect of HAc concentration on the corrosion rate of X-65 carbon steel in bubbling CO ₂ solutions (0 – 5000 ppm HAc, pH 4, 1000 rpm 22°C).	35
Figure 14. The effect of HAc concentration on the cathodic potentiodynamic sweeps and Tafel slopes in bubbling CO ₂ solutions containing 0, 100 and 1000 ppm HAc (pH 4, 1000 rpm, 22°C).	36
Figure 15. The effect of HAc concentration on the anodic potentiodynamic sweeps and Tafel slopes in bubbling CO ₂ solutions containing 0, 100 and 1000 ppm HAc (pH 4, 1000 rpm, 22°C).	36
Figure 16. The effect of pH on the potentiodynamic sweeps in bubbling CO ₂ solutions containing 100 ppm HAc (1000 rpm, 21°C).	37
Figure 17. The effect of rotational velocity on the potentiodynamic sweeps in bubbling CO ₂ solutions containing 100 ppm HAc at varying velocities (pH 4, 21°C).	38
Figure 18. The effect of temperature on the potentiodynamic sweeps in bubbling CO ₂ solutions containing 100 ppm HAc (pH 4, 1000 rpm).	39
Figure 19. The effect of temperature on the corrosion rate of X-65 carbon steel in bubbling CO ₂ solutions containing 100 ppm HAc (pH 4, 1000 rpm).	40

Figure 20. The repeatability in the potentiodynamic sweeps (100 ppm HAc, pH 4, 22°C, 1000 rpm). Note ‘a’ represents a potentiodynamic sweep measured in error.....	41
Figure 21. The effect of HAc and temperature on the corrosion rate of X-65 steel in bubbling CO ₂ solutions containing 100 ppm HAc (pH 4, 1000 rpm). Error bars represent the maximum and minimum experimental values.....	43
Figure 22. The effect of HAc concentration on the corrosion rate of X-65 steel in bubbling CO ₂ solutions (60°C, pH 4, 1000 rpm). Error bars represent the maximum and minimum experimental values.....	44
Figure 23. The effect of HAc on the corrosion rate of X-65 steel in bubbling CO ₂ solutions (60°C, pH 4, 1000 rpm). Error bars represent the maximum and minimum experimental values.....	44
Figure 24. The effect of Ca ²⁺ on the potentiodynamic sweeps of bubbling CO ₂ solutions containing 100 ppm HAc (22°C, pH 4, 1000 rpm). A-0 ppm Ca ²⁺ , B-1000, C-2000, D-4000, E-8000, F-16000.....	46
Figure 25. The effect of Ca ²⁺ in bubbling CO ₂ solutions containing 100 ppm HAc (60°C, pH 4, 1000 rpm). Error bars represent the maximum and minimum experimental values.	47
Figure 26. The effect of Ca ²⁺ concentration and pH on the corrosion rate of X-65 steel in bubbling CO ₂ solutions containing 100 ppm HAc (60°C, 1000 rpm).....	47
Figure 27. The effect of HAc and Ca ²⁺ concentration on the corrosion rate of X-65 steel in bubbling CO ₂ solutions (60°C, pH 5, 1000 rpm).	48
Figure 28. Potentiodynamic sweeps in 3% NaCl and simulated brine solutions containing 100 ppm HAc (22°C, pH 4, 1000 rpm).....	50
Figure 29. The effect of simulated brines and HAc concentration on the corrosion rate of X-65 steel in bubbling CO ₂ solutions (60°C, pH 4, 1000 rpm). Error bars represent the maximum and minimum experimental values.	50
Figure 30. Anodic factor and fitted trend line as a function of HAc concentration.	67
Figure 31. The electrochemical reactions in bubbling CO ₂ solutions containing 100 ppm HAc (22°C, pH 4, 1000 rpm).....	69
Figure 32. Comparison between the electrochemical model and experimental data in bubbling CO ₂ solutions containing 0 ppm HAc (22°C, pH 4, 1000 rpm).	69
Figure 33. Comparison between the electrochemical model and experimental data in bubbling CO ₂ solutions containing 10 ppm HAc (22°C, pH 4, 1000 rpm). ...	70
Figure 34. Comparison between the electrochemical model and experimental data in bubbling CO ₂ solutions containing 100 ppm HAc (22°C, pH 4, 1000 rpm). ..	70
Figure 35. Comparison between the electrochemical model and experimental data in bubbling CO ₂ solutions containing 1000 ppm HAc (22°C, pH 4, 1000 rpm).....	71
Figure 36. Comparison between the electrochemical model and experimental data in bubbling CO ₂ solutions containing 5000 ppm HAc (22°C, pH 4, 1000 rpm).....	71

Figure 37. Comparison between the electrochemical model and experimental data in bubbling N ₂ solutions containing 0 ppm HAc (22°C, pH 4, 1000 rpm).....	72
Figure 38. Comparison between the electrochemical model and experimental data in bubbling N ₂ solutions containing 100 ppm HAc (22°C, pH 4, 1000 rpm).....	73
Figure 39. Comparison between the electrochemical model and experimental data in bubbling N ₂ solutions containing 1000 ppm HAc (22°C, pH 4, 1000 rpm)...	73
Figure 40. Comparison between the electrochemical model and experimental data in bubbling CO ₂ solutions at 500 rpm (22°C, 100 ppm HAc, pH 4).	74
Figure 41. Comparison between the electrochemical model and experimental data in bubbling CO ₂ solutions at 1000 rpm (22°C, 100 ppm HAc, pH 4).	75
Figure 42. Comparison between the electrochemical model and experimental data in bubbling CO ₂ solutions at 2000 rpm (22°C, 100 ppm HAc, pH 4).	75
Figure 43. Comparison between the electrochemical model and experimental data in bubbling CO ₂ solutions at 4000 rpm (22°C, 100 ppm HAc, pH 4).	76
Figure 44. Comparison between the electrochemical model and experimental data in bubbling CO ₂ solutions at pH 4 (22°C, 100 ppm HAc, 1000 rpm).	78
Figure 45. Comparison between the electrochemical model and experimental data in bubbling CO ₂ solutions at pH 5 (22°C, 100 ppm HAc, 1000 rpm).	78
Figure 46. Comparison between the electrochemical model and experimental data in bubbling CO ₂ solutions at pH 6 (22°C, 100 ppm HAc, 1000 rpm).	79
Figure 47. Comparison between the electrochemical model and experimental data in bubbling CO ₂ solutions at 22°C (100 ppm HAc, pH 4, 1000 rpm).	80
Figure 48. Comparison between the electrochemical model and experimental data in bubbling CO ₂ solutions at 40°C (100 ppm HAc, pH 4, 1000 rpm).	80
Figure 49. Comparison between the electrochemical model and experimental data in bubbling CO ₂ solutions at 80°C (100 ppm HAc, pH 4, 1000 rpm).	81
Figure 50. Comparison between the experimental data and electrochemical and GDN models at 22°C (0-5000 ppm HAc, pH 4, 1000 rpm).....	83
Figure 51. Comparison between the experimental data and electrochemical and GDN models at 40°C (0-5000 ppm HAc, pH 4, 1000 rpm).....	84
Figure 52. Comparison between the experimental data and electrochemical and GDN models at 60°C (0-5000 ppm HAc, pH 4, 1000 rpm).....	85

List of Tables

Table 1-1. Coefficients in the mass transport correlation equation	17
Table 2-1. Test matrix for the research	19
Table 3-1. Chemical composition of 5LX65 steel (wt %).....	24
Table 5-1. Comparison between calculated reaction limiting currents and the experimental limiting currents. (Note “—“ denotes no data available).....	57
Table 5-2. Comparison between calculated mass-transfer limiting currents and experimental limiting currents. (Note “—“ denotes no data available).....	58

1. Introduction

The economics of oil and gas production are a complicated endeavor. One of the major decisions made before a well is drilled is the material of construction for the pipeline. At the heart of this decision is an estimate of the lifetime of the well. Carbon steel is usually the material of choice because it is available in most countries, easy to weld or install, and less expensive than corrosion resistant alloys. On the other hand, carbon steel corrodes in the multiphase (oil/water/gas) mixtures it transports and an acceptable corrosion allowance must be determined. If carbon steel cannot be used, and corrosion resistant alloys must be employed, a company may not see a return on their capital investment until much later in the well's lifetime, which may make some wells unattractive to produce.

Since oil wells are being produced farther and farther offshore, companies have found it more profitable to link several pipelines to a single separation facility. This production scheme exposes the pipeline to the produced multiphase mixture for long distances and the flow regime and corrosion rate may change throughout the pipeline. During initial production from a well, the multiphase mixture contains mostly oil and a gas phase consisting of natural hydrocarbons, carbon dioxide and nitrogen. Brine can also be present in small amounts and the amount produced increases as the well ages. Dissolved in the oil is a mixture of organic compounds, which can include paraffins, waxes, and organic acids.

The presence of organic acids in oil and gas lines was first discovered in 1944 (Crolet 1999). At that time, the concept of the organic acids present in the undissociated

and dissociated form was not known. Early analysis of organic acids was done on the basis of molecular weight, which did not allow for a distinction between acetic, propanoic, butyric, etc. Today, the concept of organic acids present in oil field brines in either the undissociated or dissociated form and forming a buffer system is better understood. However, analysis of oil field brines for anions and cations determination, especially bicarbonates in the presence of acetates, is still a problem for companies today.

In the past two decades, pipeline corrosion investigations and predictions have concentrated on “sweet” CO₂ corrosion by looking at effects of the partial pressure of carbon dioxide, temperature, pH and hydrodynamics on the system. The partial pressure of carbon dioxide is one of the main parameters used to determine the corrosiveness of a multiphase mixture to carbon steel. But, a relationship to accurately predict corrosion from the partial pressure of carbon dioxide has eluded researchers for many years. From the field, it is known that produced fluids rich in carbon dioxide (5 to 10 bar) are almost always corrosive regardless of what the acetic acid (HAc) concentration. But fluids produced at low partial pressures of CO₂ can be significantly corrosive when small amounts (6–60 ppm) of HAc are present (Crolet 1999).

Before discussing the findings of CO₂ corrosion of mild steel in the presence of HAc, a brief introduction to CO₂ corrosion will be given.

1.1. CO₂ Corrosion

Research into the corrosion mechanisms of carbon dioxide and its effects on mild steel under varying conditions of pressure, temperature, pH and oil-water fractioning has been done by de Waard et al. (1975, 1991, 1993, 1995), Dugstad et al. (1994) and Nesic

et al. (1994, 1995, 2001). They have proposed models to predict carbon dioxide corrosion of mild steel based on the results of their work. The following reactions are a summary of the knowledge available in the open literature.

First, carbon dioxide gas dissolves into water to form carbonic acid through hydration by water.



The carbonic acid then dissociates to form bicarbonate which itself can further dissociate



According to de Waard and Milliams (1975) the reduction of the undissociated acid molecule (H_2CO_3) occurs after it is absorbed onto the metal surface. This is the rate-determining step of the process, so the corrosion rate of the metal surface is directly related to the concentration of the undissociated acid in solution.

Two possible cathodic reactions occur in the corrosion process



while a single anodic reaction occurs



Whether or not the direct reduction of carbonic acid (1.5) actually occurs on the metal surface is debated since it could be argued that carbonic acid would dissociate into a hydrogen ion faster than it could diffuse to the surface of the steel. If carbonic acid

dissociates in the boundary layer, then it would only act as an additional source of hydrogen ions and the only cathodic reaction in the corrosion process is Reaction 1.6.

It has also been shown that the solubility of iron carbonate in salt water decreases with an increase in system temperature. This iron carbonate precipitate may form a protective film depending on the solution composition, pressure, and temperature of the system. The overall reaction in the corrosion process can then be written as



Other corrosion products are possible with the presence of chlorides, sulfides, oxygen etc. in either the liquid or gas phase.

The effect of flow on corrosion when no protective films are present is through increased mass transport of the corrosion species to the metal surface (Nesic 1996). When the mass transport of the species is not fast enough to support the electrochemical process, limiting currents result. On the other hand, accumulation, saturation, and precipitation can result at the metal surface if the transport of the species away from the surface is limited. If the corrosion process is under charge transfer (activation control) or chemical reaction control, then changes in the flow will have no effect on the corrosion rate since mass transfer is not the limiting step.

1.2. Acetic Acid Corrosion

When a gaseous phase of HAc is present in multiphase pipelines (or from the dissociation of an acetate compound to form HAc), it, in addition to carbon dioxide, dissolves into the aqueous solution. The HAc then dissociates into hydrogen and acetate ions



Since HAc is a stronger acid than carbonic acid (pKa 4.76 vs 6.35 at 25°C), it is the main source of hydrogen ions when the two acid concentrations are similar. The acetate ions form iron acetate upon reaction with iron



Moreover, iron acetate's solubility is much higher than iron carbonate's, so protective film formation by iron acetate does not readily occur. Without formation of a stable protective film, the corrosion rates of the steel remain at a high value.

Some understanding of the role of HAc in CO₂ corrosion comes from field experience as related to the so-called Top-of-Line-Corrosion (Gunaltun 2000). But, very few systematic studies have been performed in the laboratory. Little or no information exists about the basic effect of HAc on the anodic and cathodic reactions. Hedges and McVeigh (1999) reported a mild increase in the cathodic reaction in the presence of HAc although their results were not fully conclusive. The work of Crolet et al. (1999) suggests that the presence of HAc inhibits the anodic (iron dissolution) reaction.

Garsany et al. (2002) published work using voltammetry to study the effect of acetate ions on the rates and mechanisms of corrosion using a rotating disc electrode (RDE) on film-free surfaces. Their voltammograms show two waves, which are attributed to hydrogen ion and HAc reduction on the steel surface. They argue that since HAc dissociation can occur very quickly it is not possible to distinguish the reduction of hydrogen ions from direct HAc reduction at the electrode surface.

Crolet et al. (1999) were of some of the first to report on low concentrations of HAc (6-60 ppm) affecting the corrosion rates of carbon steel. They argue that the increase in the rate of corrosion in the presence of HAc occurs due to an inversion in the bicarbonate/acetate ratio. At this inversion point, HAc is the predominant acid compared to carbonic acid and is therefore the main source of acidity.

Hedges and McVeigh (1999) published results on acetate's role in CO₂ corrosion. Experiments using both HAc and sodium acetate as a source of acetate ions in various media (3% NaCl and 2 synthetic oilfield brines) were performed using rotating cylinder electrodes. Both sources of acetate ions were shown to increase the corrosion rate, but acetic acid decreased the pH while sodium acetate increased it. The increased corrosion rates were attributed to the forming of thinner iron carbonate films since acetate ions have the ability to form iron acetate and transport iron away from the steel surface. However, no attempt was made to quantify the thickness or morphology of the films formed in their experiments.

Joosten et al. (2002) performed additional experiments using acetic acid, synthetic seawater, and an oil phase in glass cells. They found that acetic acid increased the corrosion rate by decreasing the pH, but the system could be inhibited very effectively (below 400 ppm HAc). Effective inhibition has also been reported by Hedges et al. The most important feature of the Joosten et al. work is the presence of pitting on the 13% Cr electrodes. This material would be the likely material chosen for service if X-65 was found unacceptable. However, no pits were found on a Super 13% Cr material under the test conditions (600 ppm HAc and 95°C).

1.3. Rotating Cylinders

Electrodes have been rotated since 1905 to provide some quantitative control over solution convection (Gabe 1998). Multiple electrode geometries have been employed (rotating wire (WRE), rotating-disc (RDE), rotating-cylinder (RCE), rotating cone (RconE) and rotating hemisphere (RHSE)), but only the RCE and RDE have found widespread use in industry and laboratories. One of the main differences between the two geometries is the flow regime each generates upon rotation. The RDE is characterized predominantly by laminar flow, while the RCE is mainly turbulent. The Reynolds number is used as the transition criteria for hydrodynamics and the Sherwood number as a mass transport coefficient in the correlation $Sh \propto Re^n$. For rotating cylinders, the mass transfer correlation of Eisenberg (1954) is most appropriate:

$$Sh = \frac{k_m d_c}{D} = 0.0791 \times Re^{0.7} \times Sc^{0.356} \quad (1.11)$$

where Sh is the Sherwood number, k_m is the mass transfer coefficient of hydrogen in m/s, d_c is the cylinder diameter in m, D is the diffusion coefficient in m^2/s , and Sc is the Schmidt number.

Coefficients for the mass transport correlation for other geometries are given in Table 1-1 (Gabe 1998).

Table 1-1. Coefficients in the mass transport correlation equation

Geometry	n (laminar)	n (turbulent)	Re (criteria)
RDE	0.5	0.8	1×10^5
RConE	0.45	0.90	2×10^4
RHSE	0.5	0.67	1×10^4
RCE	0.33	0.67	2×10^2

The main features of the RCE (Gabe 1998) which provide its unique experimental characteristics are:

1. Generates turbulent flow at $Re > 2 \times 10^2$, which is exceeded at relatively low rotation rates.
2. Potential and current densities are uniform, which promotes uniform reaction rates over the electrode surface.
3. Mass transport is high and can be enhanced by the use of roughened surfaces.
4. The mass transport equations are well established.
5. Superimposed axial flow does not usually alter the mass transfer control.

Experimental studies of the corrosion rate in a rotating cylinder electrode (RCE) system can provide information much more quickly and inexpensively than flow loops. Another advantage of the RCE is that all of the transport equations involved in the corrosion process can be solved analytically if laminar flow is present. Even in turbulent flow, the mass transfer and momentum equations can be formulated at least as well as in straight sections of pipe (Gabe 1998). However, a simple expression to relate corrosion rate data between the RCE and flow loops has not been found. If the assumption of equal mass transfer rates is made, then empirical correlations between the linear velocity in pipe flow and the rotational speed of the electrode can be found.

2. Test Matrix and Research Objectives

Based on previous research, some of the principal questions that need to be asked are:

1. What are the main effects of HAc on the anodic and cathodic reactions present in CO₂ corrosion?
2. What are the effects of oil-field brines on the anodic and cathodic reactions present in CO₂ corrosion when HAc is present?
3. What is the best way to integrate the findings about the HAc effect on CO₂ corrosion into a corrosion prediction model?

The following test matrix will be performed to answer the above questions.

Table 2-1. Test matrix for the research

	Objective # 1	Objective # 2	Objective # 2
Steel Type	X-65	X-65	X-65
Solution	3% NaCl	3% NaCl	Simulated Brine
De-oxygenation Gas	CO ₂ , N ₂	CO ₂	CO ₂
Ca ²⁺ Conc (ppm)	0	0 – 16,000	0
HAc Conc (ppm)	0 – 5000	0, 100	0, 100
T (°C)	22, 40, 60, 80	22, 60	22, 60
Rotation Velocity (rpm)	500 – 4000	1000	1000
pH	4, 5, 6	4, 5	4, 5
Measurement Techniques	Potentiodynamic Sweeps, LPR, EIS, WL	Potentiodynamic Sweeps, LPR, EIS, WL	Potentiodynamic Sweeps, LPR, EIS, WL

Where LPR is the linear polarization resistance technique, EIS is the electrochemical impedance spectroscopy and WL is the weight loss method for corrosion rate determination.

All of the permutations in the experimental matrix were not performed. Whenever a parameter was varied, the other parameters were set to their baseline values of 22°C,

100 ppm HAc, pH 4.00 and 1000 rpm. For example, in the HAc concentration study, the HAc concentration was varied from 0 – 5000 ppm but the temperature remained constant at 22°C, the system pH was maintained at 4 and the rotational velocity was set to 1000 rpm.

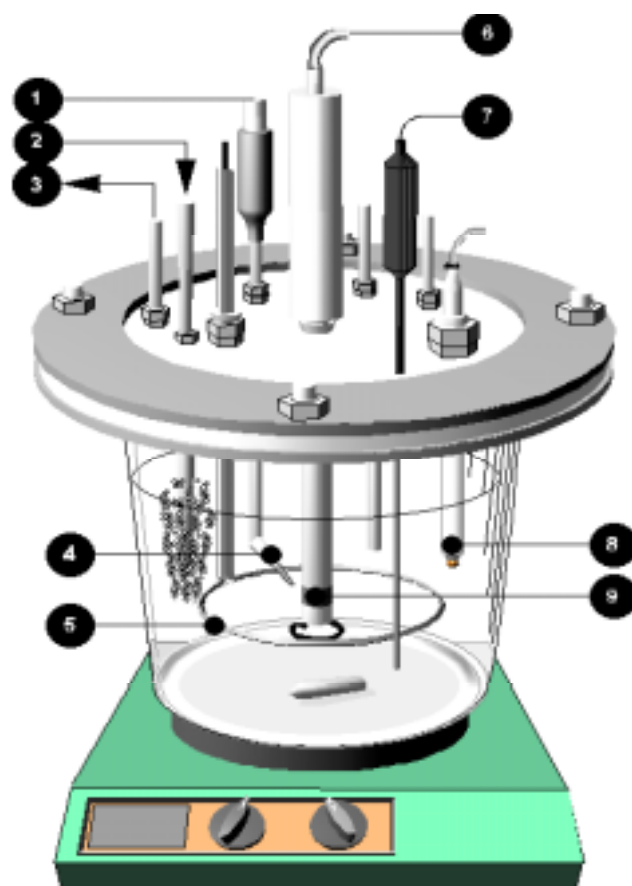
It should be noted that the pH and temperatures have been chosen to perform the potentiodynamic sweeps under conditions where corrosion product film formation is unlikely. The weight loss experiments, in a similar manner, will be performed for short periods of time (24 hours) to avoid significant film formation.

3. Experimental Setup

A schematic of the experimental cell is shown in Figure 1. To begin, the experimental apparatus was assembled, a salt solution was prepared, added to the cell, and then de-oxygenated for one hour using carbon dioxide gas. The test temperature was set using a hot plate and controlled using a feedback temperature probe. Once de-oxygenation had occurred and the test temperature was reached, the appropriate amount of HAc was then added to the cell and de-oxygenation continued for an additional 30 minutes. Since HAc is volatile and the bubbling CO₂ gas could strip the HAc out of the test cell, a preconditioning cell was used. The preconditioning cell was kept constant at the test temperature and contained the same fluid composition as the experimental cell. The preconditioning cell ensured the CO₂ entering the experimental cell was saturated with HAc and H₂O vapor.

The pH meter used in the experiments was calibrated at the test temperature by heating of the buffer solutions. The pH was monitored before and after the HAc addition to ensure the fluid composition was similar between test runs. In order to achieve the desired system pH, minute adjustments were made using droplets of hydrochloric acid and sodium bicarbonate. The electrode was then immersed into the test solution and the electrode's rotational velocity was set. After approximately 30 additional minutes, electrical connections were made and measurements started. The experimental measurements were typically conducted in the same order. First, the corrosion rate was measured using LPR, then the solution resistance was found using electrochemical

impedance spectroscopy (EIS). The cathodic and then the anodic potentiodynamic sweeps were then performed.



- | | |
|-------------------------|----------------------|
| 1. Reference Electrode | 6. Rotator |
| 2. Gas In | 7. Temperature Probe |
| 3. Gas Out | 8. pH Probe |
| 4. Luggin Capillary | 9. Working Electrode |
| 5. Pt Counter Electrode | |

Figure 1. Schematic of the test cell.

3.1. Potentiodynamic Sweeps

All electrochemical measurements were made using a Gamry PC4 monitoring system and analyzed using the accompanying software. The potentiodynamic sweeps were conducted at a sweep rate of 0.2 mV/s and the solution resistance was manually corrected after measurement using EIS. Potentiodynamic sweeps were conducted at constant pH with the pH adjustment occurring after each sweep. During the anodic sweep for example, the system pH was set to 4.00 ± 0.01 and the sweep started. Due to iron dissolution, the pH of the system may rise to 4.08 by the end of the sweep. The pH was then adjusted using HCl before the beginning of the next sweep. Anodic sweeps were limited to polarization less than 200 mV above the corrosion potential to limit excessive iron concentrations in the test cell.

The potentiodynamic sweeps were always conducted starting from the corrosion potential. For example, a cathodic potentiodynamic sweep would scan from the corrosion potential to approximately -650 mV below the corrosion potential. The corrosion potential would then be allowed to drift back to the starting corrosion potential before an anodic potentiodynamic sweep was performed. The LPR measurements were taken at ± 5 mV around the corrosion potential. The working electrode was machined from the parent material and had a diameter of 1.20 cm and an area of 5.4 cm^2 . The composition of the X-65 mild steel (as reported by Metal Samples) used in the experiments is shown in Table 3-1.

Table 3-1. Chemical composition of 5LX65 steel (wt %)

Al	Cr	Mo	S	V	B	Cu	Nb	Si
0.032	0.011	0.103	0.004	0.055	0.0002	0.010	0.030	0.240
C	Fe	Ni	Sn	Ca	Mn	P	Ti	
0.150	balance	0.020	0.005	0.0032	1.340	0.011	0.001	

3.2. Weight Loss Experiments

After the solution had come to the desired temperature and the pH was adjusted, a pre-weighed electrode was immersed into the solution. During the twenty-four hour weight loss experiments, the pH was adjusted approximately every hour or two, which corresponded with LPR measurements. After twenty-four hours, the electrodes were taken out of the test solution, rinsed with alcohol, wiped with a soft cloth to remove any corrosion product, and then weighed after drying.

4. Results and Discussion

4.1. Water Chemistry Calculations

The water chemistry of the experimental solutions was found by solving the equilibrium expressions for all of the reactions given in Chapter 1. Expressions for the equilibrium constants are those used in Nescic's (2002) mechanistic model. The concentrations of some of the species at 1 bar CO₂, 22°C and 10 ppm HAc is shown in Figure 2. The concentration of dissolved carbon dioxide and carbonic acid is fixed with the pressure and temperature of the system and is not a function of pH. Most of the experimental work was performed at pH 4 and it is evident that when 10 ppm HAc is present in solution, HAc is the main source of acidity up to a pH of approximately 4.7. When 100 ppm HAc is present, under the same conditions, it is the main source of acidity up to a pH of almost 6. This is shown in Figure 3.

In the work presented here, the concentration of HAc will be discussed on the amount added to the system. For example, when 100 ppm HAc is added to the system and the pH adjusted to 4, the undissociated concentration of HAc is 85 ppm but when experiments were performed the same addition of HAc to the system resulted in an undissociated concentration of 6 ppm. The undissociated concentration of HAc as a function of pH is shown in Figure 4.

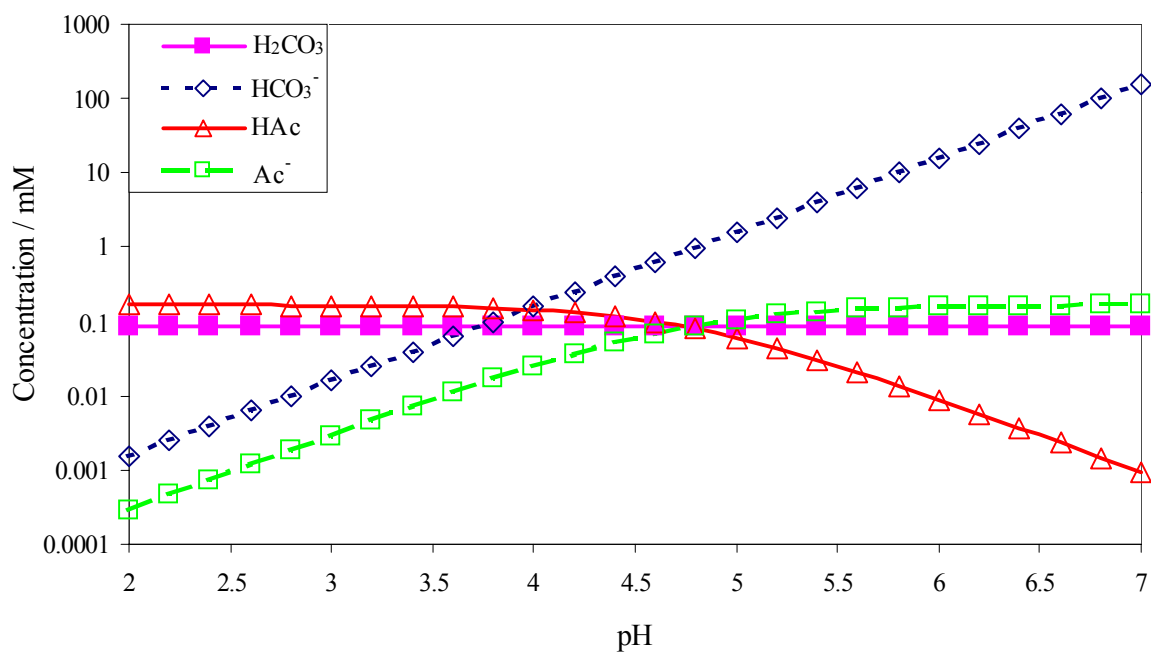


Figure 2. The effect of pH on the concentration of species at 1 bar CO₂, 22°C and 10 ppm HAc added.

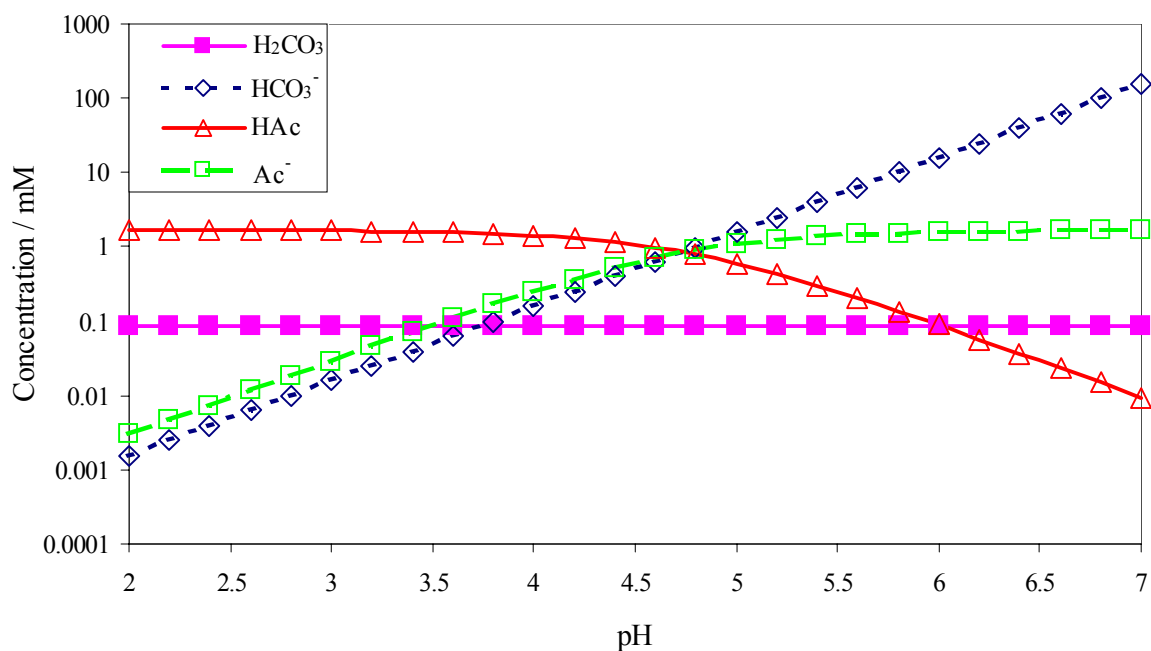


Figure 3. The effect of pH on the concentration of species at 1 bar CO₂, 22°C and 100 ppm HAc added.

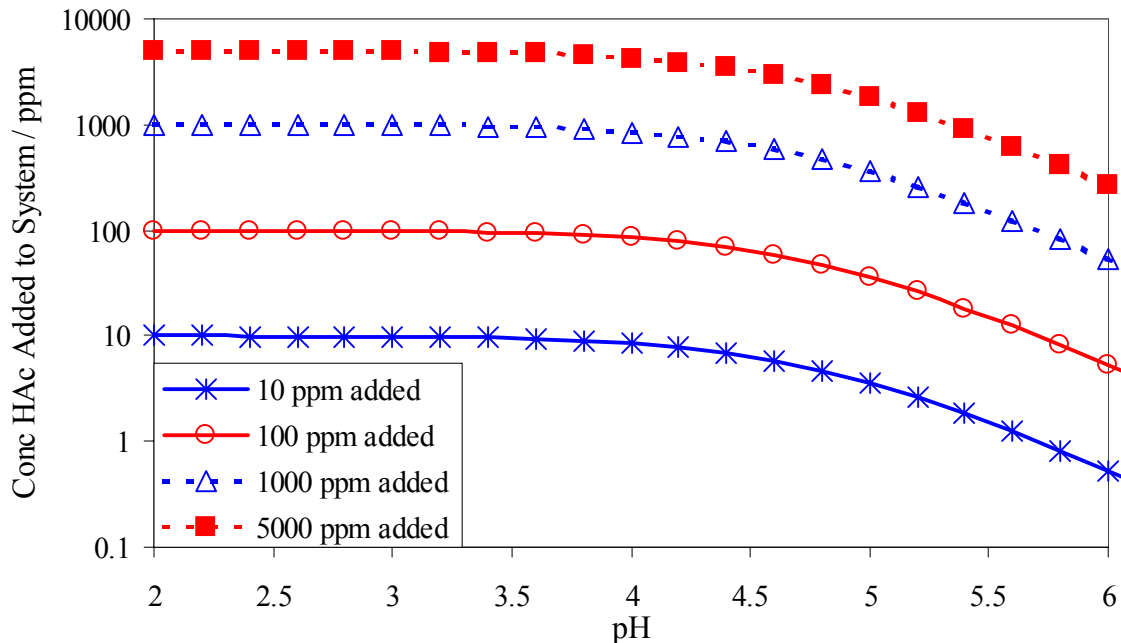


Figure 4. The concentration of undissociated HAC as a function of concentration added and system pH at 22°C.

4.2. The Effect of HAC In Solutions De-Oxygenated Using N₂ and CO₂

Initially, potentiodynamic sweeps were performed in 3% sodium chloride solutions flushed with nitrogen for a concentration range of 0 to 1000 ppm HAC at pH 4 and the results are shown in Figure 5. The pH was held constant to distinguish the effect of the acetic species from the effect of H⁺ on the cathodic and anodic reactions. At a constant pH, the concentration of hydrogen ions is fixed, and the effect of the acetic species on the cathodic and anodic reactions could be seen. There is a clear acceleration of the cathodic limiting current density with increased concentrations of HAC. The anodic reaction was inhibited with an increase in the HAC concentration, which has also been reported by Crolet (1999). Since the straight portion of the cathodic sweep (at low overpotentials) did not move significantly with increasing concentrations of HAC, this

suggests that reduction of hydrogen ions is more likely occurring rather than direct reduction of HAc. For example, if HAc were reduced at the surface as a new reaction, then the charge transfer cathodic reaction would be expected to increase 1000 times with an increase in HAc concentration from 0 to 1000 ppm. Also, when the concentration of HAc is increased from 0 ppm to 1000 ppm, the limiting current is accelerated almost 30 times.

The corrosion rates measured by LPR and Tafel analysis are shown in Figure 6. It should be stressed that the corrosion rates measured using LPR were taken within approximately 30-45 minutes of exposure to the test solution. The corrosion rates were estimated using a cathodic Tafel slope of 120 mV/dec and an anodic Tafel slope of 80 mV/dec when HAc is present and 40 mV/dec when HAc is not present. The corrosion rates estimated using these two methods are similar since the cathodic and anodic reactions are most likely under charge-transfer control for the hydrogen ion reaction. In the case of an increase in HAc concentration from 0 to 100 ppm, the limiting current increased almost nine times (Figure 5) while the corrosion current did not increase much. This indicates that HAc acts primarily as a source of hydrogen ions and does not affect the charge transfer reactions. Garsany et al. (2001) also have reported HAc acting as a source of hydrogen ions.

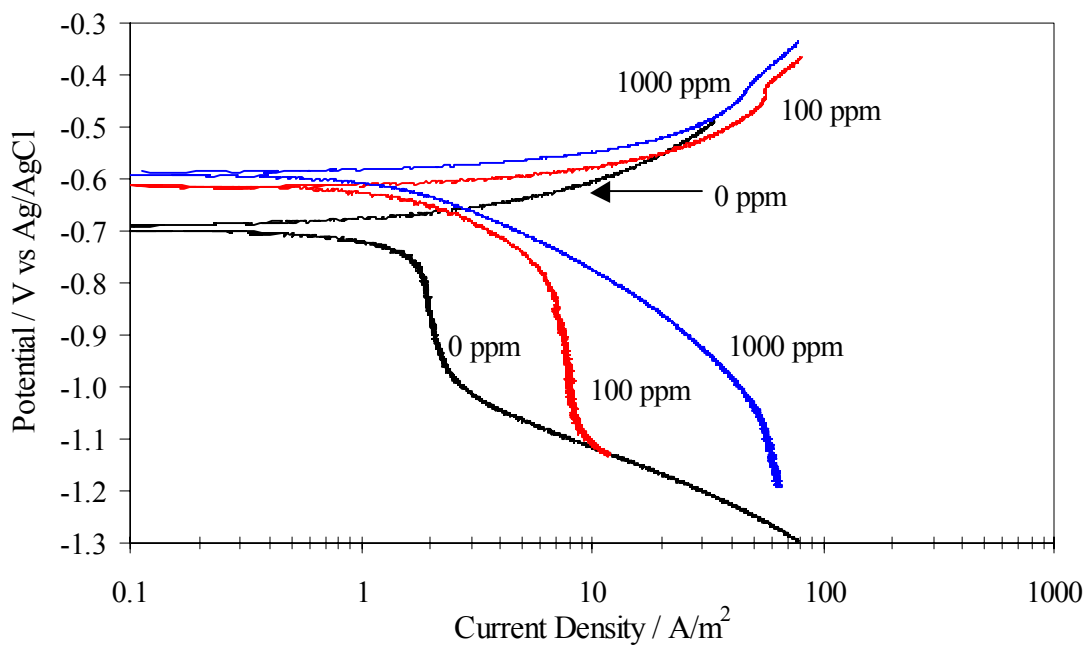


Figure 5. Potentiodynamic sweeps in bubbling N_2 solutions containing 0, 100, and 1000 ppm HAc (pH 4, 1000 rpm, 22°C).

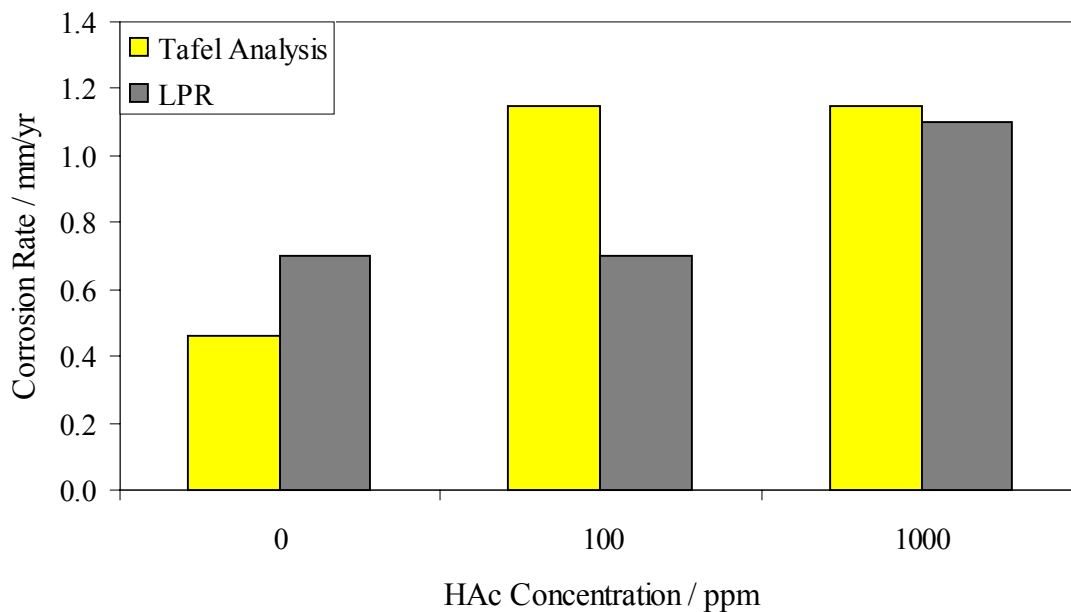


Figure 6. The effect of HAc concentration on the corrosion rate of X-65 steel in bubbling N_2 solutions (pH 4, 1000 rpm, 22°C).

The effect of adding carbon dioxide was studied at the same concentrations of HAc. The results for the 0 ppm HAc concentrations are shown in Figure 7. It is evident from Figure 7 that the limiting current density of the cathodic reaction is increased slightly in the presence of carbon dioxide. The anodic reaction in nitrogen solutions was unaffected by an addition of carbon dioxide at all concentrations of HAc.

The 100 and 1000 ppm HAc potentiodynamic sweeps are shown in Figure 8 and 9, respectively. At 100 ppm of HAc, the limiting current densities of the cathodic reactions for both solutions are significantly increased when compared to the 0 ppm HAc limiting current densities. Again a slight increase in the limiting current density of the cathodic reaction in the presence of carbon dioxide was found. A similar trend is found upon a further increase in the HAc concentration to 1000 ppm.

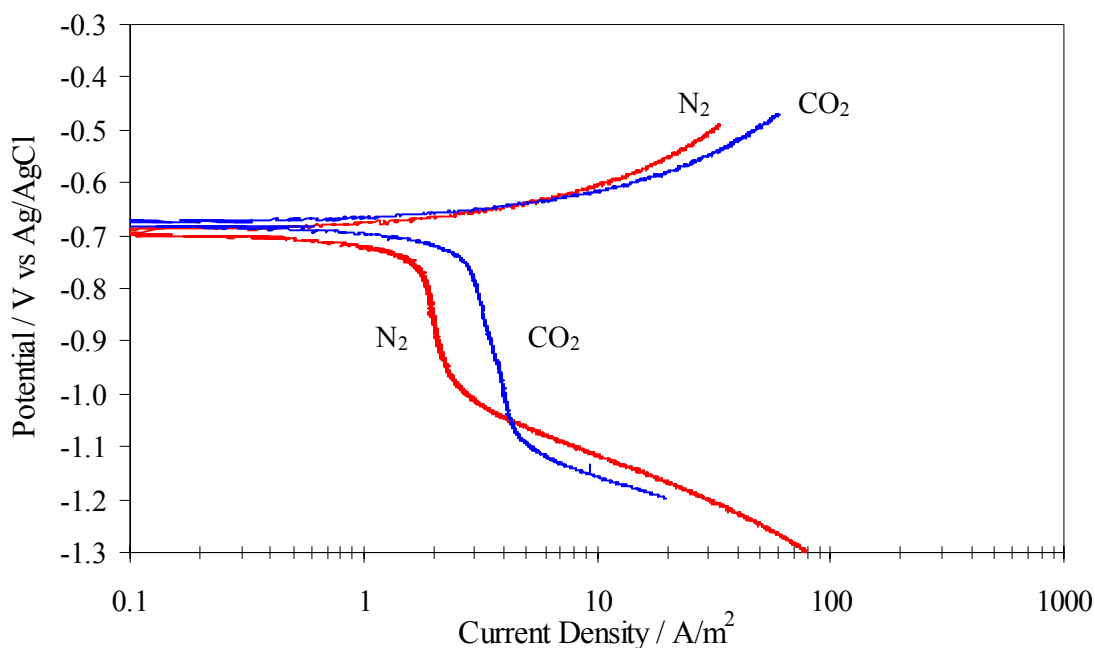


Figure 7. Comparison between potentiodynamic sweeps in bubbling CO₂ and N₂ solutions containing 0 ppm HAc (pH 4, 1000 rpm, 22°C).

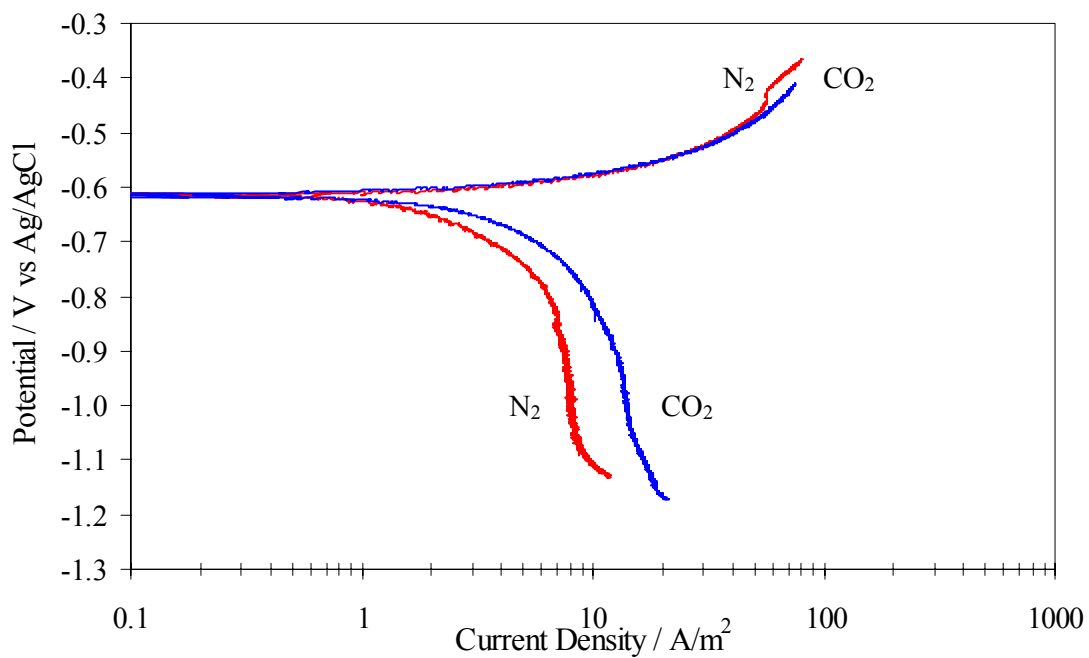


Figure 8. Comparison between potentiodynamic sweeps in bubbling CO₂ and N₂ solutions containing 100 ppm HAc (pH 4, 1000 rpm, 22°C).

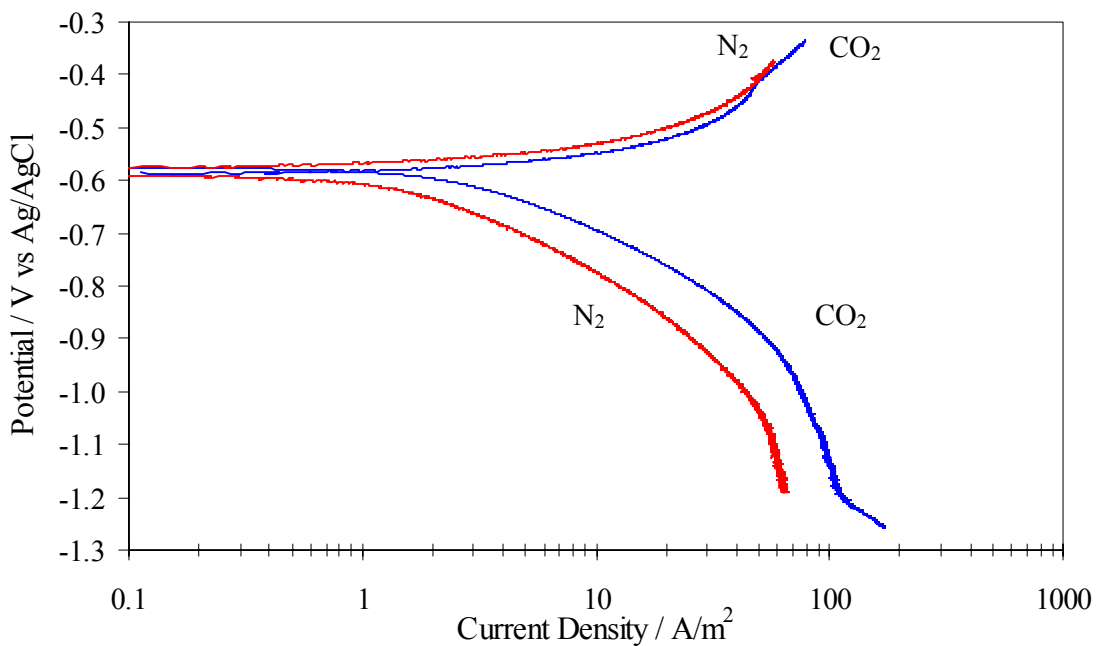


Figure 9. Comparison between potentiodynamic sweeps in bubbling CO₂ and N₂ solutions containing 1000 ppm HAc (pH 4, 1000 rpm, 22°C).

4.3. The Effect of HAc Concentration in the Presence of Carbon Dioxide

The effect of HAc concentration was studied in 3% sodium chloride solutions adjusted to a pH of 4. The HAc concentration was varied from 0 to 5000-ppm and the cathodic and anodic sweeps are shown in Figures 10 and 11, respectively. The particular concentrations were selected since these values are typically encountered in service. As argued above, with increasing concentrations of HAc, the limiting current of the cathodic reaction is accelerated. However, with increasing concentrations of HAc, the anodic reaction is retarded.

Nyquist impedance plots for 3% sodium chloride solutions containing 0 ppm and 100 ppm HAc at pH 4 are shown in Figure 12. Polarization resistance values (R_p), as measured using LPR, are also shown in Figure 12 and agree well with the intercept of the real axis on the Nyquist plot. In both cases, the impedance plots exhibit a depressed semi-circle at high frequencies, which indicates a charge-transfer process and an inductive loop at low frequencies. A depressed semi-circle is indicative of a double-layer capacitance and is common for iron dissolution in an acidic media. It has been suggested (McCafferty 1997, MacDonald 1982) that the surface roughness and non-uniform distribution of the current density of the metal surface may be responsible for the depression. The inductive loop at low frequencies indicates the iron dissolution mechanism may occur in multiple steps with intermediate species. The process is not completely mass transfer controlled since no Warburg diffusion impedance was present.

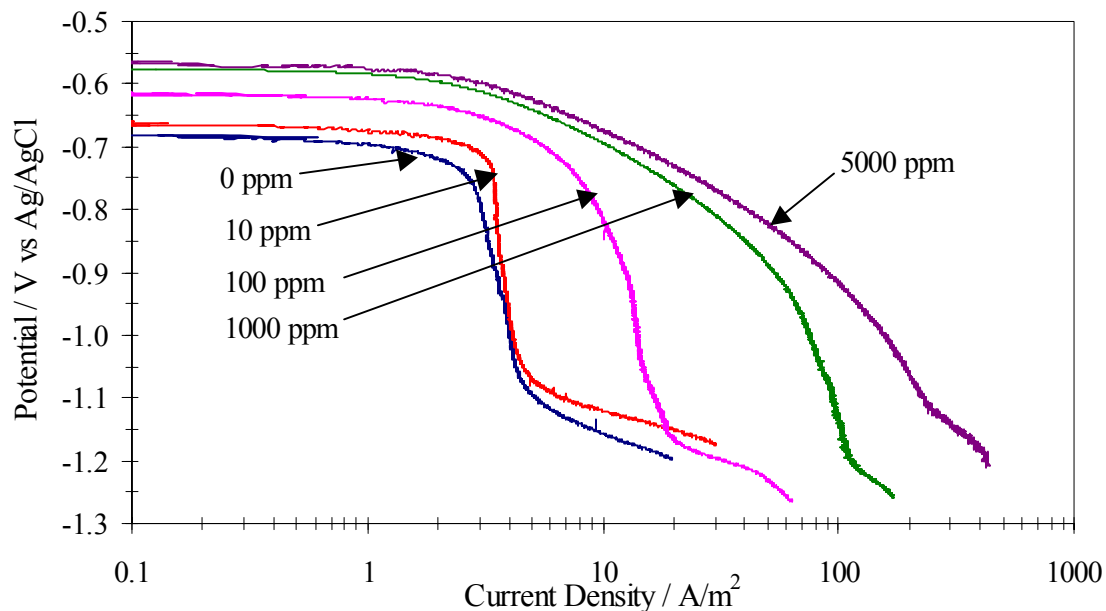


Figure 10. The effect of HAc concentration on the cathodic potentiodynamic sweeps in bubbling CO₂ solutions (0 – 5000 ppm HAc, pH 4, 1000 rpm, 22°C).

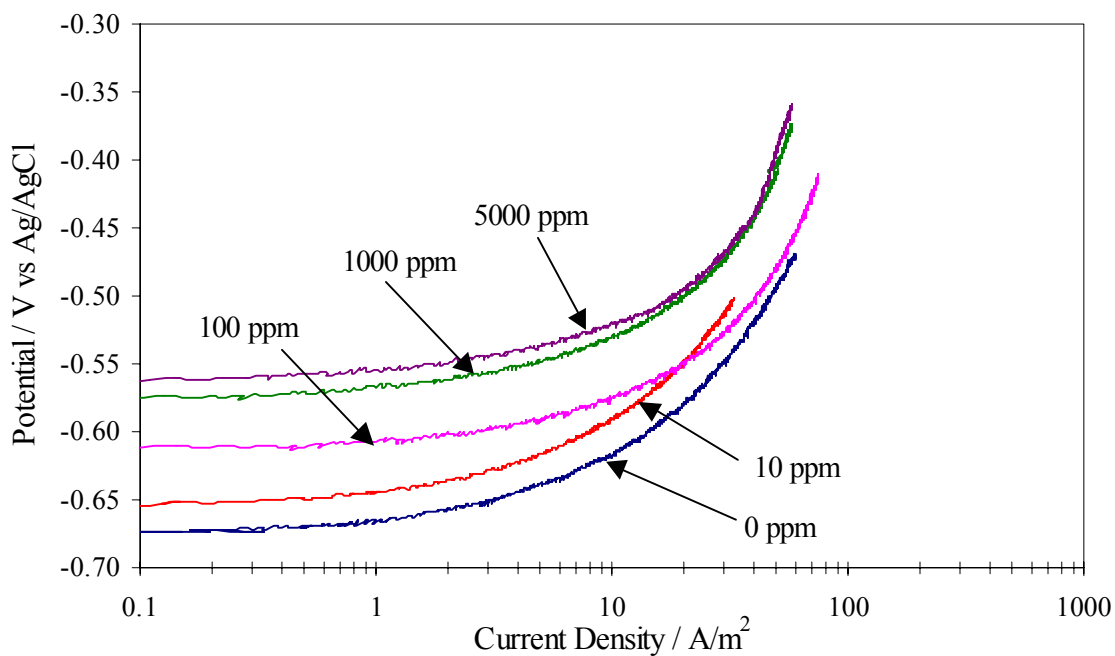


Figure 11. The effect of HAc concentration on the anodic potentiodynamic sweeps in bubbling CO₂ solutions (0 – 5000 ppm HAc, pH 4, 1000 rpm, 22°C).

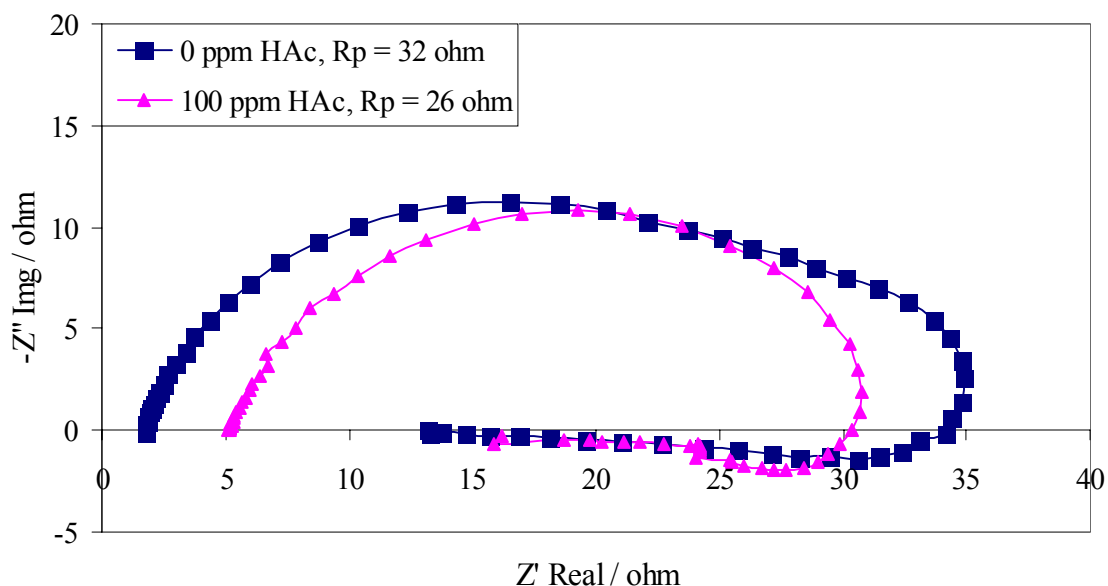


Figure 12. The effect of HAC concentration on the Nyquist impedance plots in bubbling CO₂ solutions. (0, 100 ppm HAC, pH 4, 1000 rpm, 22°C).

The effect of HAC concentration on the CO₂ corrosion rate is shown in Figure 13. As before, the LPR measurements were taken within 30-45 minutes of electrode exposure to the test solution. As in cases where no CO₂ was present (Figure 6), the corrosion rates are approximately the same when HAC is present, since the HAC is acting only as an extra source of hydrogen and the reactions are under charge-transfer control so availability of hydrogen ions is not rate limiting. Selected potentiodynamic sweeps containing varying concentrations of HAC, which have already been shown in Figures 9 and 10, have been shown again in Figures 14 and 15, with the fitted Tafel slopes used in the LPR calculation. The anodic Tafel slope was found to be 40 mV/dec when HAC is not present and 80 mV/dec when HAC was present. These Tafel slopes were found to best approximate the potentiodynamic sweeps and the extrapolated corrosion rates under all

conditions studied. Since HAc is acting only as a source of hydrogen ions, the cathodic slope was found to be 120 mV/dec at 22°C and agreed with the experimental data.

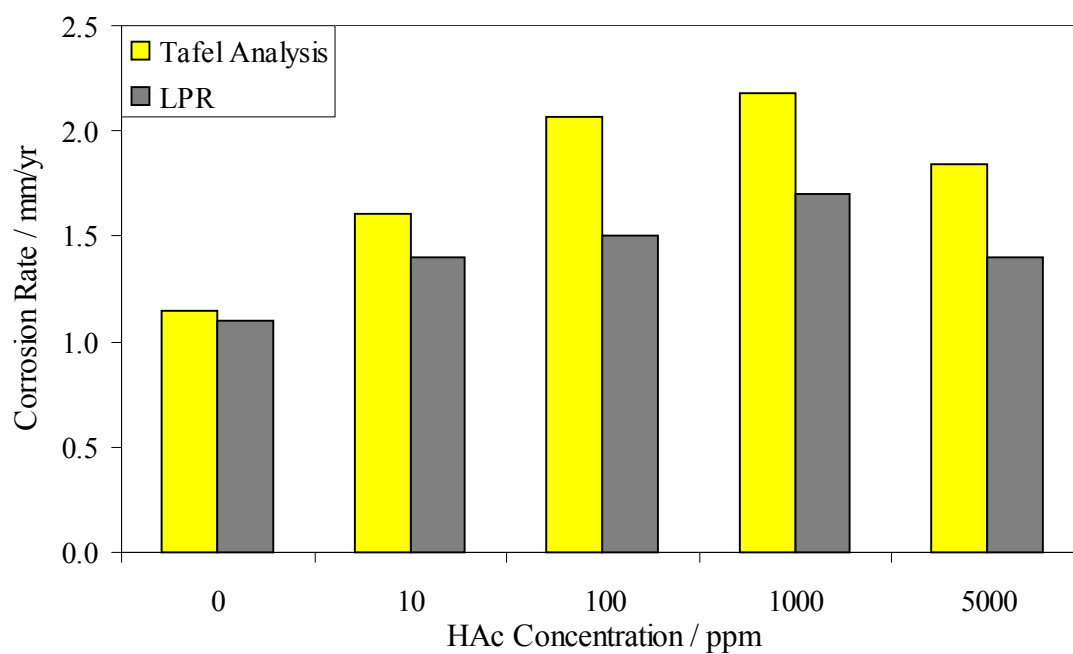


Figure 13. The effect of HAc concentration on the corrosion rate of X-65 carbon steel in bubbling CO₂ solutions (0 – 5000 ppm HAc, pH 4, 1000 rpm 22°C).

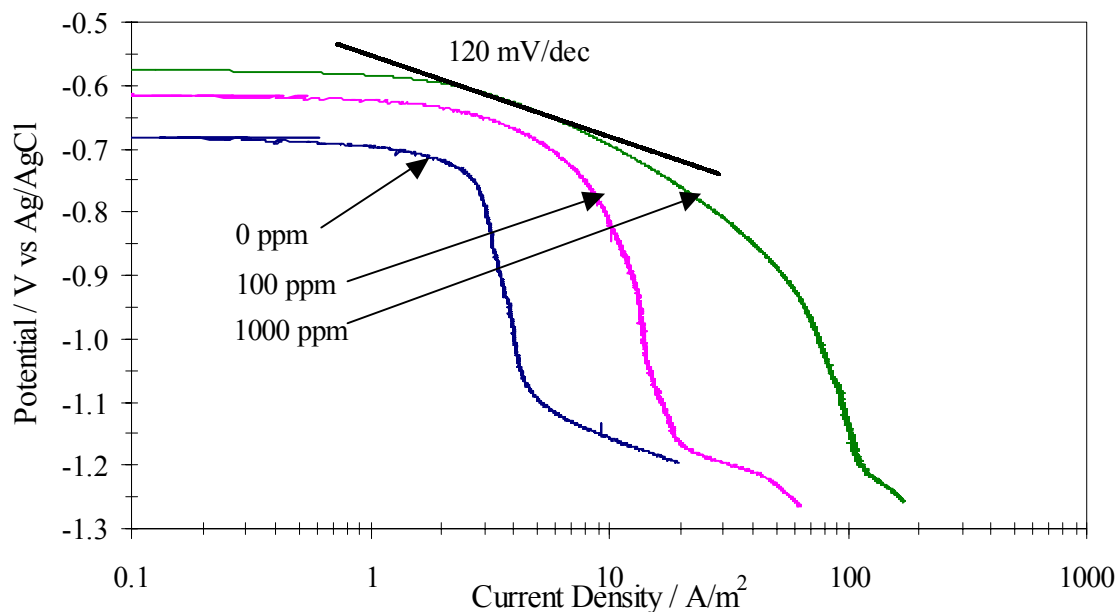


Figure 14. The effect of HAC concentration on the cathodic potentiodynamic sweeps and Tafel slopes in bubbling CO₂ solutions containing 0, 100 and 1000 ppm HAC (pH 4, 1000 rpm, 22°C).

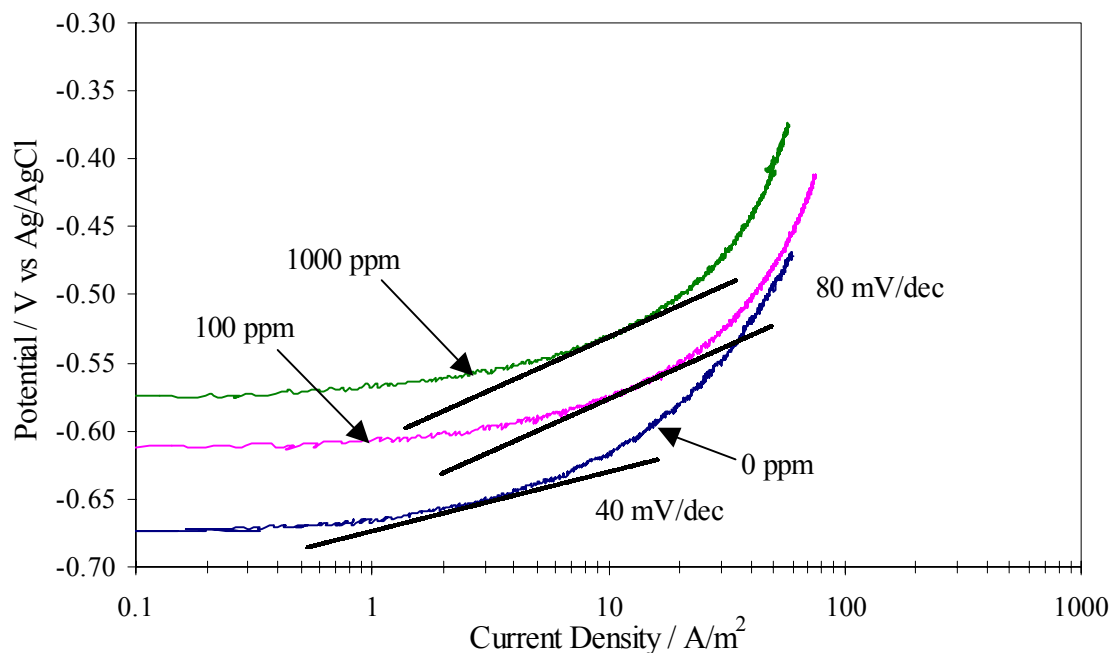


Figure 15. The effect of HAC concentration on the anodic potentiodynamic sweeps and Tafel slopes in bubbling CO₂ solutions containing 0, 100 and 1000 ppm HAC (pH 4, 1000 rpm, 22°C).

4.4. The Effect of pH

The effect of pH on the potentiodynamic sweeps was studied in 3% sodium chloride solutions with 100 ppm HAC adjusted in the pH range of 4 to 6. The results are shown in Figure 16. As the pH is increased from 4 to 5, the anodic reaction rate is increased. But a further increase in pH from 5 to 6 does not result in a further increase in the anodic reaction rate. According to Bokris (1973), the hydroxyl molecule (OH^-) acts as a catalyst in the dissolution step for iron. At higher pH, the surface of the steel is saturated with the hydroxyl molecules and the rate-limiting step is the iron leaving the metal lattice. This saturation with hydroxyl molecules in carbon dioxide solutions occurs between a pH of 4 and 5. On the other hand, the cathodic reaction is retarded by each increase in pH due to less hydrogen ions being available for reduction proving again that HAC acts solely as a source of hydrogen ions only.

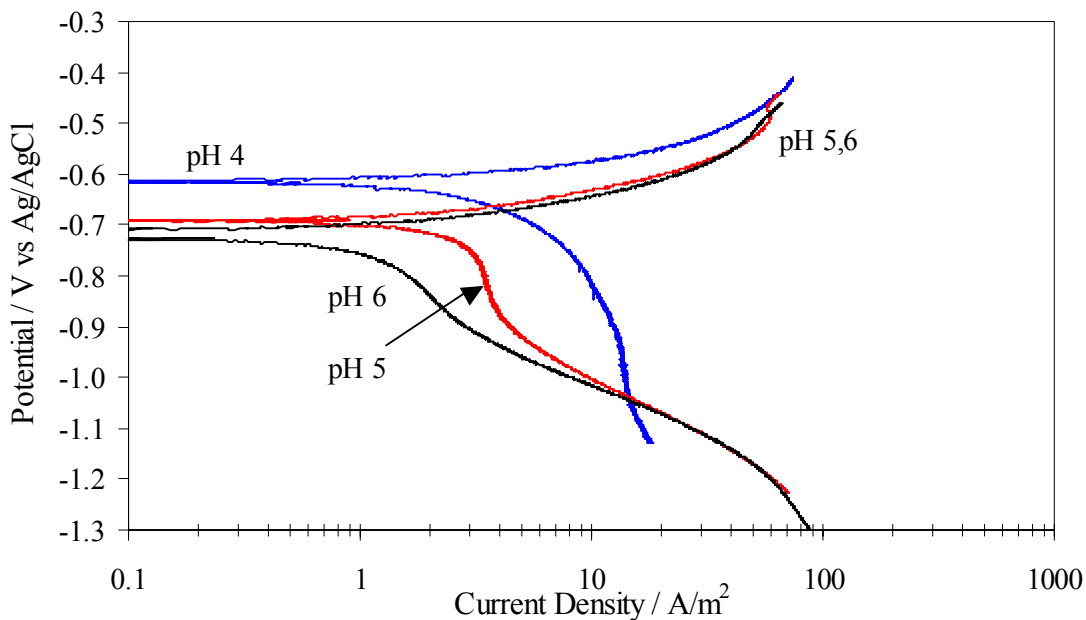


Figure 16. The effect of pH on the potentiodynamic sweeps in bubbling CO_2 solutions containing 100 ppm HAC (1000 rpm, 21°C).

4.5. The Effect of Rotational Velocity

The effect of velocity (500-4000 rpm) was studied using potentiodynamic sweeps performed in 3% sodium chloride solution, 100 ppm HAc and at pH 4. The results are shown in Figure 17. According to theory, the mass-transfer limiting currents should increase by a factor of 1.6 with each doubling of velocity since the Reynolds number term, in the Sherwood number correlation, is raised to the 0.7 power (Equation 1.11). The increase in the limiting current is measured to be approximately 1.8-2 when the velocity is doubled. The corrosion potential, as well as the anodic reaction, does not change with velocity suggesting a constant corrosion rate. This appears to support the assumption that the corrosion rate under the conditions studied is charge transfer controlled.

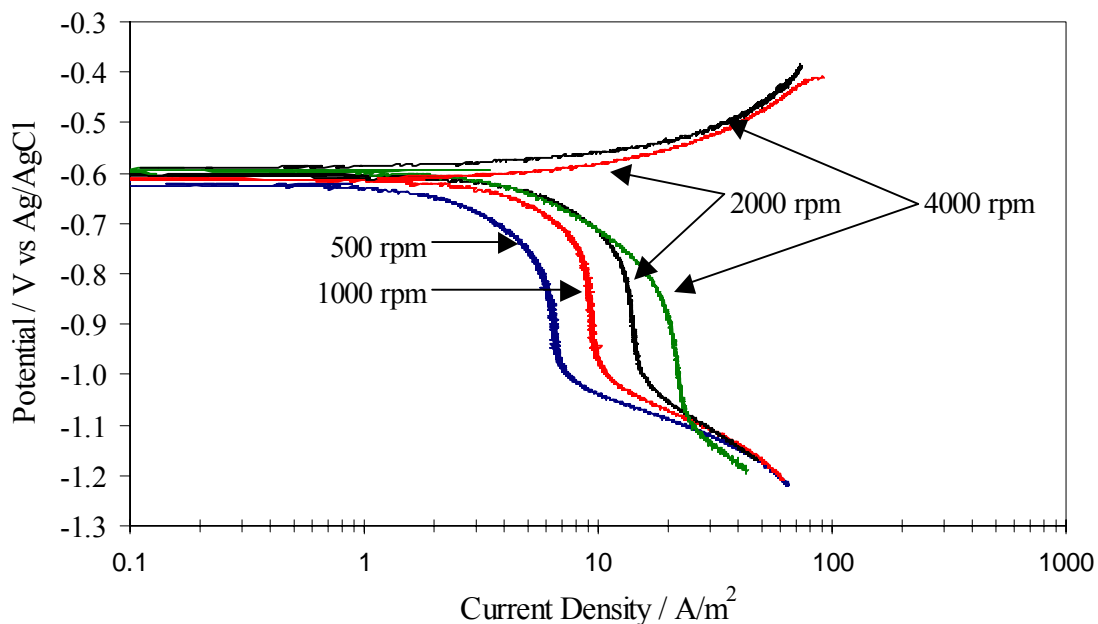


Figure 17. The effect of rotational velocity on the potentiodynamic sweeps in bubbling CO₂ solutions containing 100 ppm HAc at varying velocities (pH 4, 21°C).

4.6. The Effect of Temperature

The effect of temperature on the potentiodynamic sweeps was studied in 3% sodium chloride solutions containing 100 ppm HAc at pH 4. The results are shown in Figure 18. There is a clear acceleration of both the cathodic and anodic reaction rates with an increase in temperature, as is expected. Also, with an increase in temperature, the corrosion potential is shifted to more negative values due to the anodic reaction rate increasing more than the cathodic one. The corrosion rates measured by LPR and calculated from Tafel slopes are shown in Figure 19 and the two methods are in good agreement.

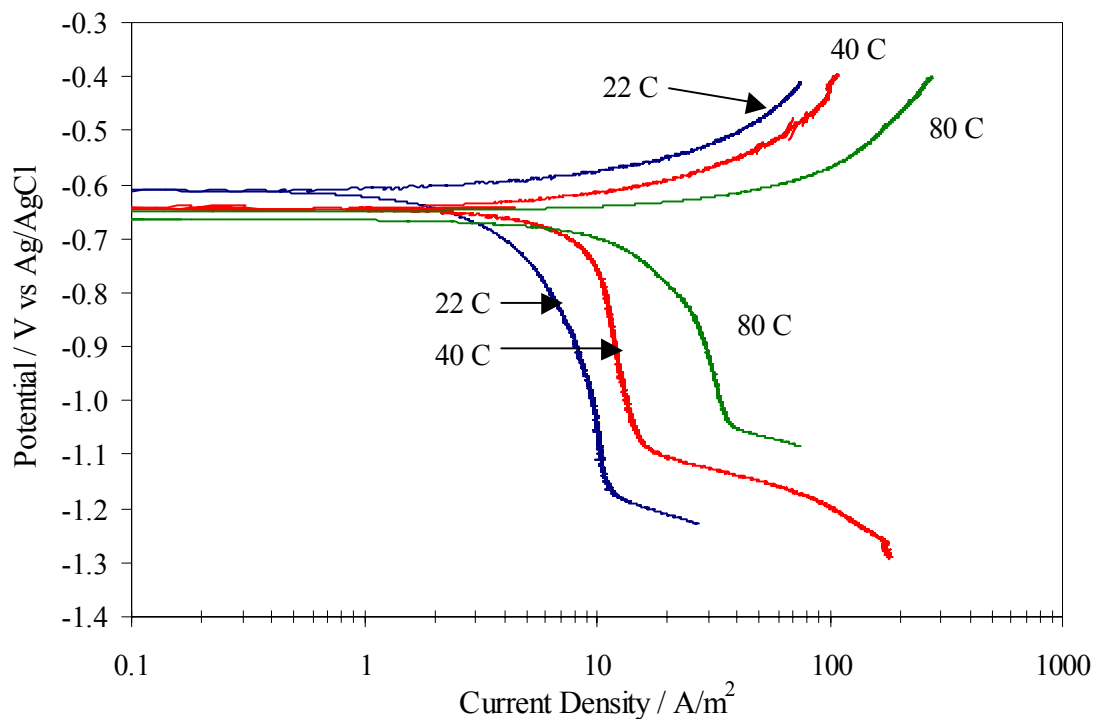


Figure 18. The effect of temperature on the potentiodynamic sweeps in bubbling CO₂ solutions containing 100 ppm HAc (pH 4, 1000 rpm).

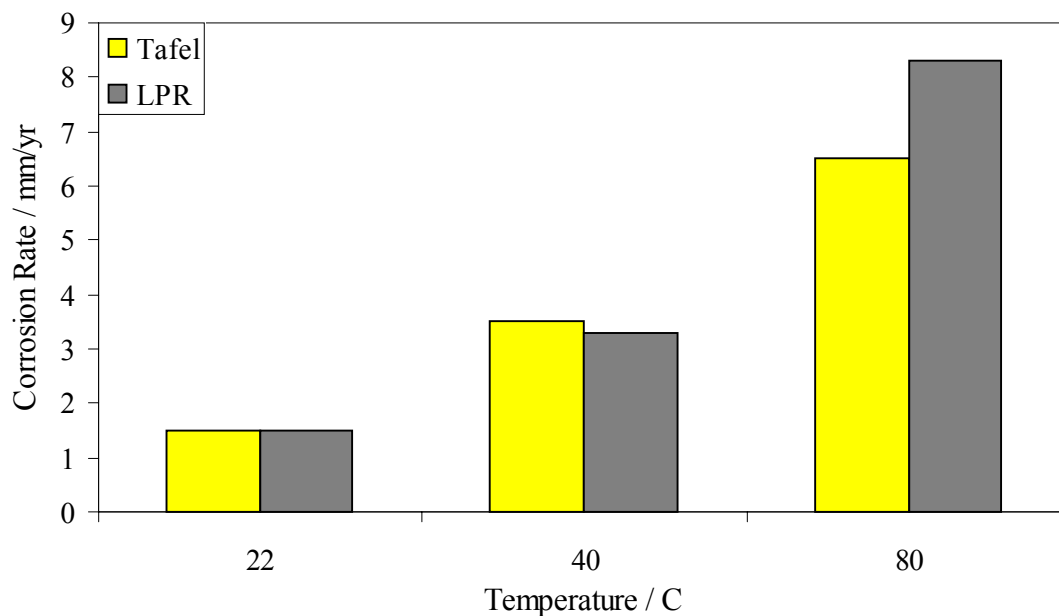


Figure 19. The effect of temperature on the corrosion rate of X-65 carbon steel in bubbling CO₂ solutions containing 100 ppm HAc (pH 4, 1000 rpm).

4.7. Repeatability of Potentiodynamic Sweeps

Rather than theoretically estimating the error in the potentiodynamic sweeps, a single experiment was performed multiple times to show the range in experimental values. The experimental potentiodynamic sweeps are shown in Figure 20. It is evident that the cathodic potentiodynamic sweep can have varying shapes, which is probably due to the activation of the metal surface during the experiment and a range of limiting currents can be observed. One of the potentiodynamic sweeps (labeled “a” in Figure 20) shows very high current densities near the corrosion potential. It was experimentally observed that this phenomenon typically occurred when the metal surface filmed or turned black during the sweep. It is unknown why such a small perturbation around the corrosion potential would cause such drastic changes to the metal surface. The

experimental limiting currents have an average value 9.4 with a standard deviation of 1.6. The anodic potentiodynamic sweeps typically were more reproducible between experiments and three are shown in Figure 20 with one possible outlier. The agreement between the corrosion potentials in all of the experiments is very good.

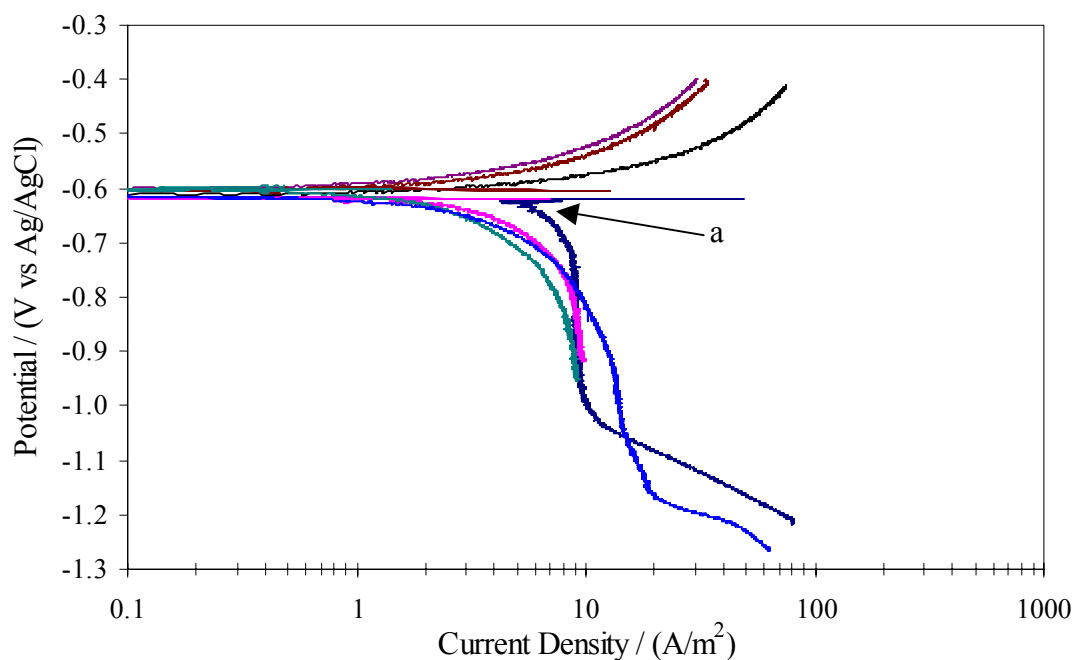


Figure 20. The repeatability in the potentiodynamic sweeps (100 ppm HAc, pH 4, 22°C, 1000 rpm). Note 'a' represents a potentiodynamic sweep measured in error.

4.8. Weight Loss Experiments

A series of weight loss experiments was initiated to verify the effect of temperature and HAc on the corrosion of carbon steel in 3% sodium chloride solutions and the results are shown in Figure 21. The average value of the method used is presented and the error bars represent the maximum and minimum experimental values. The number above the error bars represents the number of experiments used to calculate the average value. This format will be repeated in the following charts. The values presented for the LPR method are time-averaged over the course of the experiment. Some weight loss experiments were performed using no electrochemistry to see if, by measuring the corrosion rate using LPR, the system was disturbed enough to change the corrosion rate measured by weight loss. Electrochemistry, by LPR, was not found to affect the corrosion rates measured by weight loss.

The effect of increasing temperature on the corrosion rate in solutions containing 0 ppm and 100 ppm HAc measured in 3% sodium chloride solutions is shown in Figure 21. It is evident that the corrosion rates measured using LPR and by weight loss are not in perfect agreement, even when HAc is not present. As the temperature increases, the influence of HAc is more pronounced. For example, at 22°C, adding 100 ppm HAc increases the corrosion rate approximately 30%, while at 60°C the same increase in HAc concentration doubles the corrosion rate.

The effect of adding HAc to 3% sodium chloride solutions at pH of 4 and at 60°C is shown in Figure 22. It is evident that even a 10 ppm HAc addition to the solution affects

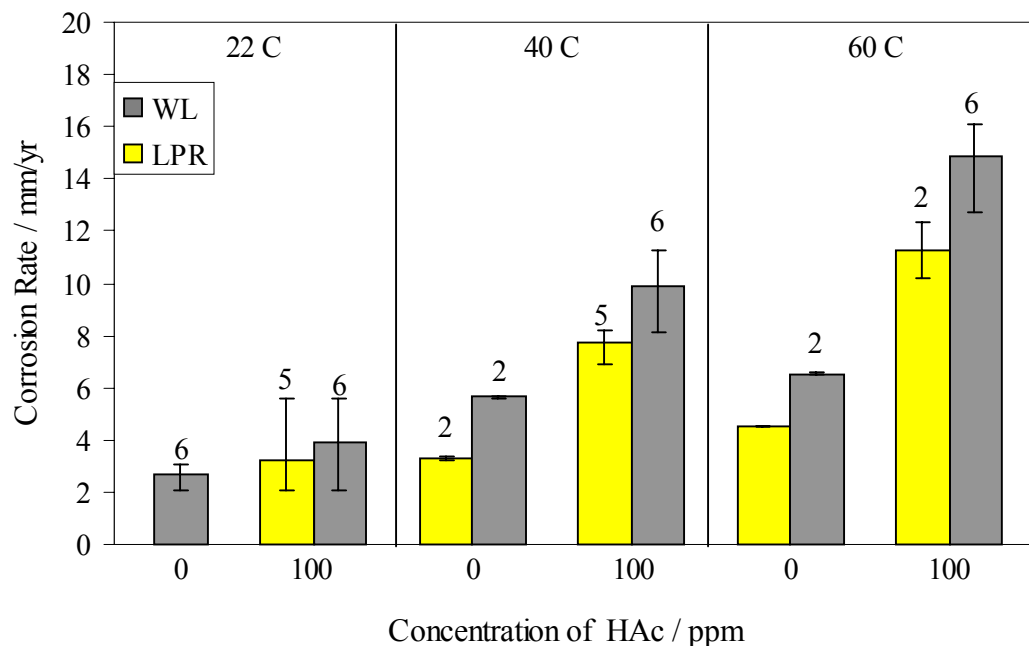


Figure 21. The effect of HAc and temperature on the corrosion rate of X-65 steel in bubbling CO₂ solutions containing 100 ppm HAc (pH 4, 1000 rpm). Error bars represent the maximum and minimum experimental values.

the corrosion rate. An increase in the HAc concentration to 1000 ppm is shown in Figure 23. It is worth noting that the 1000 ppm HAc, 24-hour weight loss experiment was performed four times. In two of the tests, weight loss measurements on the order of approximately 45 mm/yr were observed and these results are presented in Figure 23. In the other two experiments, the samples experienced pitting corrosion. No discernable difference between the four experiments can be found to identify the trigger for the pitting corrosion.

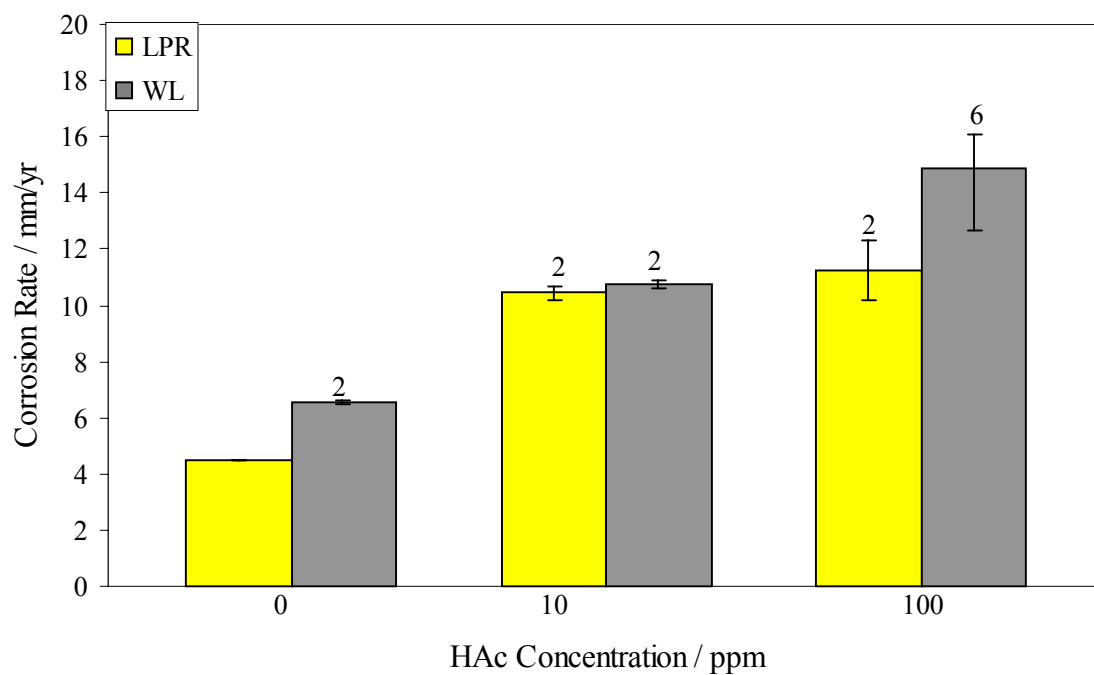


Figure 22. The effect of HAc concentration on the corrosion rate of X-65 steel in bubbling CO₂ solutions (60°C, pH 4, 1000 rpm). Error bars represent the maximum and minimum experimental values.

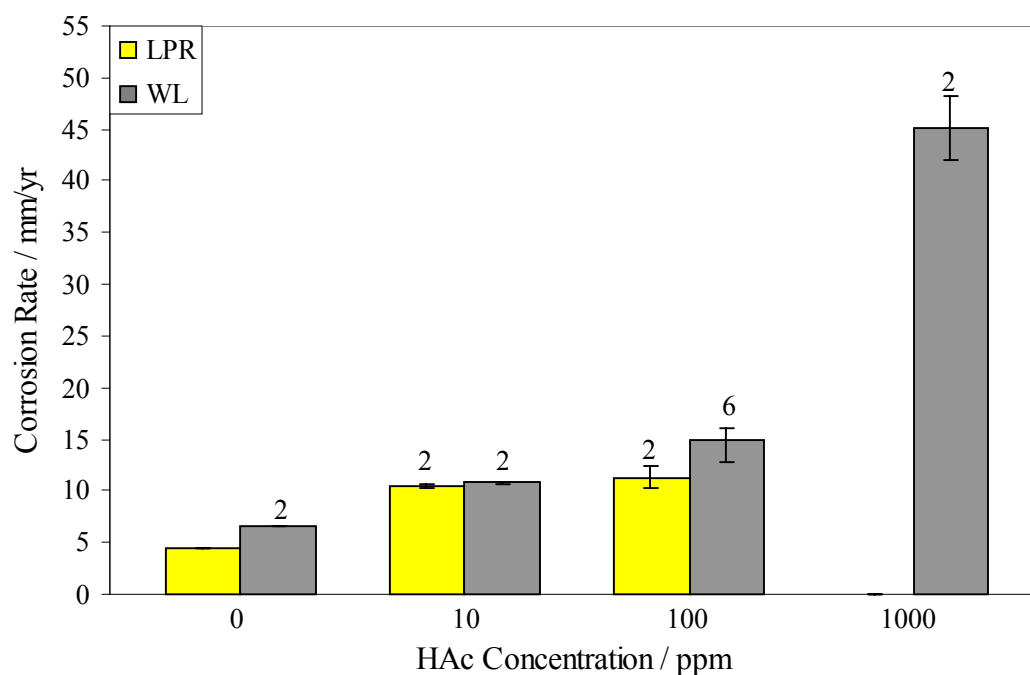


Figure 23. The effect of HAc on the corrosion rate of X-65 steel in bubbling CO₂ solutions (60°C, pH 4, 1000 rpm). Error bars represent the maximum and minimum experimental values.

4.9. The Effect of Ca^{2+}

Before adding the influence of multiple ions to solutions containing HAc, potentiodynamic sweeps were employed to find the effect of adding Ca^{2+} ions. There have been reports of high concentrations of Ca^{2+} ions lowering the corrosion rates of mild steel when no HAc is present (Crolet 1999). The potentiodynamic sweeps were performed in 3% sodium chloride solutions at pH 4 containing 100 ppm HAc. The source of Ca^{2+} ions was solid calcium chloride (CaCl_2). The results of the potentiodynamic sweeps are shown in Figure 24. It is evident that adding Ca^{2+} ions, even to very high concentrations (16,000 ppm), has little effect on the anodic reaction rate. The cathodic reaction rate, however, is mildly retarded which is probably due to scaling of the electrode as the pH increased during the potentiodynamic sweep.

A series of 24-hour weight loss experiments were performed in 3% sodium chloride solutions at pH 4 containing 100 ppm HAc and varying amounts of Ca^{2+} ions at 60°C. The results are shown in Figure 25. It is evident that a reduction in the corrosion rate is achieved when the concentration of Ca^{2+} ions reaches approximately 8000 ppm Ca^{2+} . The corrosion rate, measured using LPR and weight loss at 60°C, as a function of pH and Ca^{2+} concentration is shown in Figure 26. When the pH is increased from 4 to 5, in the presence of 100 ppm HAc, the concentration of Ca^{2+} needed for a reduction in the corrosion rate is decreased by a factor of two to 4000 ppm. For example, the corrosion rate measured by weight loss in solutions containing 4000 ppm Ca^{2+} and 100 ppm HAc, at pH 4 is approximately 17 mm/yr. At the same HAc concentration, an increase in the pH from 4 to 5 lowers the corrosion rate to approximately 8 mm/yr. An increase in the

Ca^{2+} ion concentration above 4000 ppm at pH 5 has essentially no significant affect on the corrosion rate.

The effect of HAc and Ca^{2+} ion concentration on the corrosion rate at pH 5 is shown in Figure 27. It is evident that in solutions containing no HAc, increasing amounts of Ca^{2+} lowers the corrosion rate over 50%. In solutions containing HAc (100 ppm), the corrosion rate remains at a stable value (approximately 6 mm/yr) irrespective of the Ca^{2+} concentration.

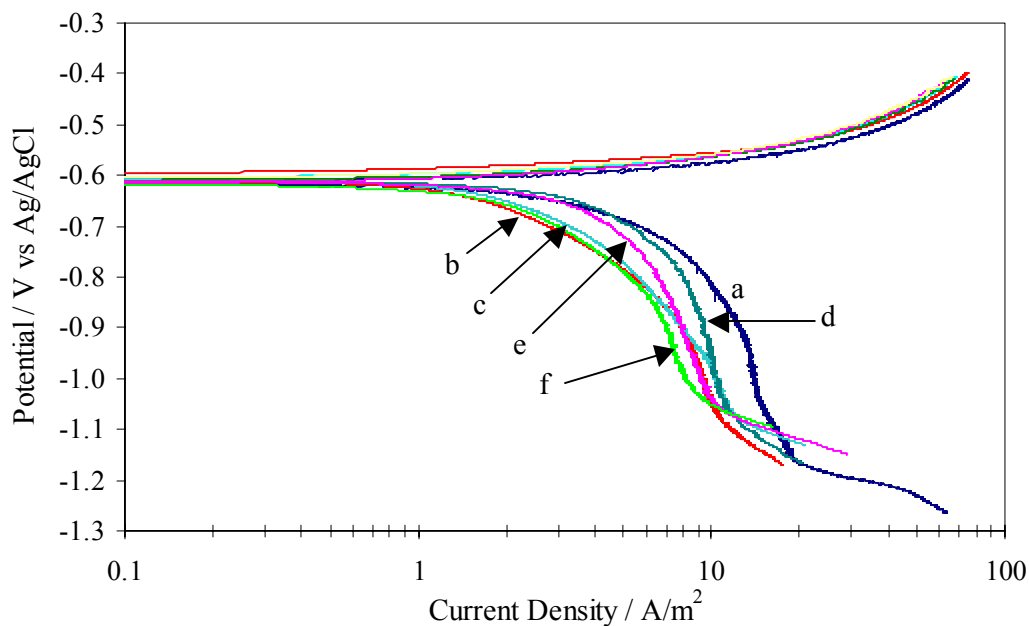


Figure 24. The effect of Ca^{2+} on the potentiodynamic sweeps of bubbling CO_2 solutions containing 100 ppm HAc (22°C, pH 4, 1000 rpm). A-0 ppm Ca^{2+} , B-1000, C-2000, D-4000, E-8000, F-16000.

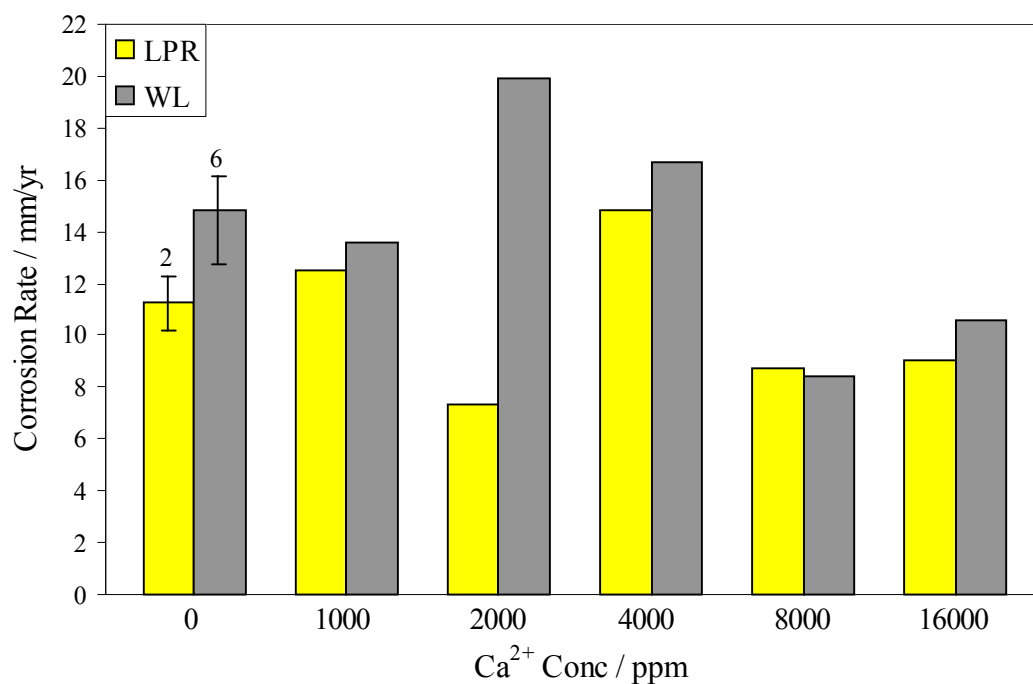


Figure 25. The effect of Ca²⁺ in bubbling CO₂ solutions containing 100 ppm HAc (60°C, pH 4, 1000 rpm). Error bars represent the maximum and minimum experimental values.

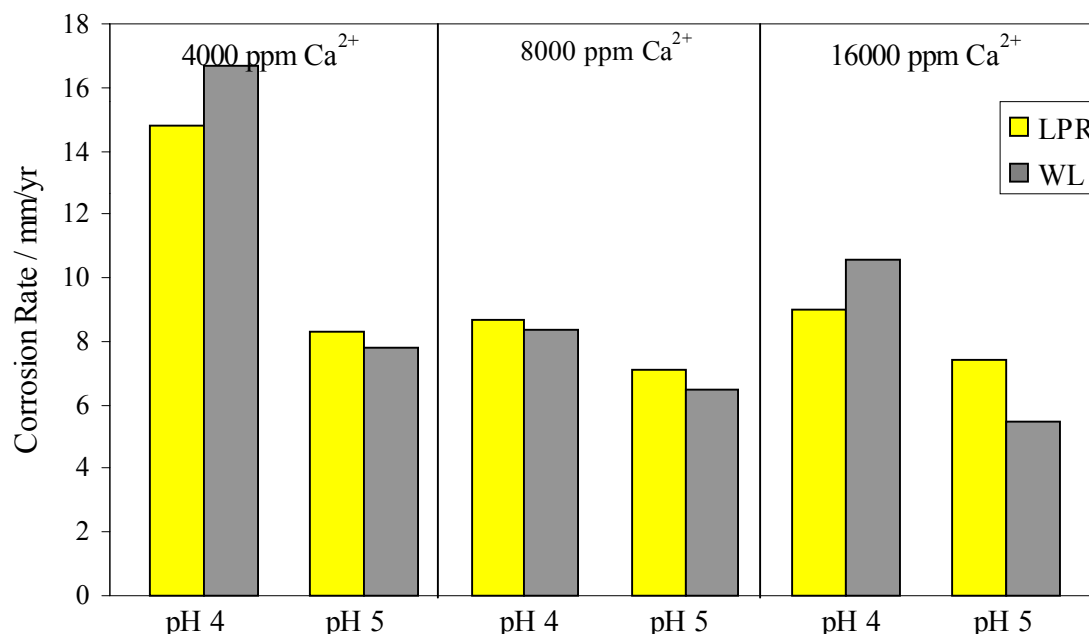


Figure 26. The effect of Ca²⁺ concentration and pH on the corrosion rate of X-65 steel in bubbling CO₂ solutions containing 100 ppm HAc (60°C, 1000 rpm).

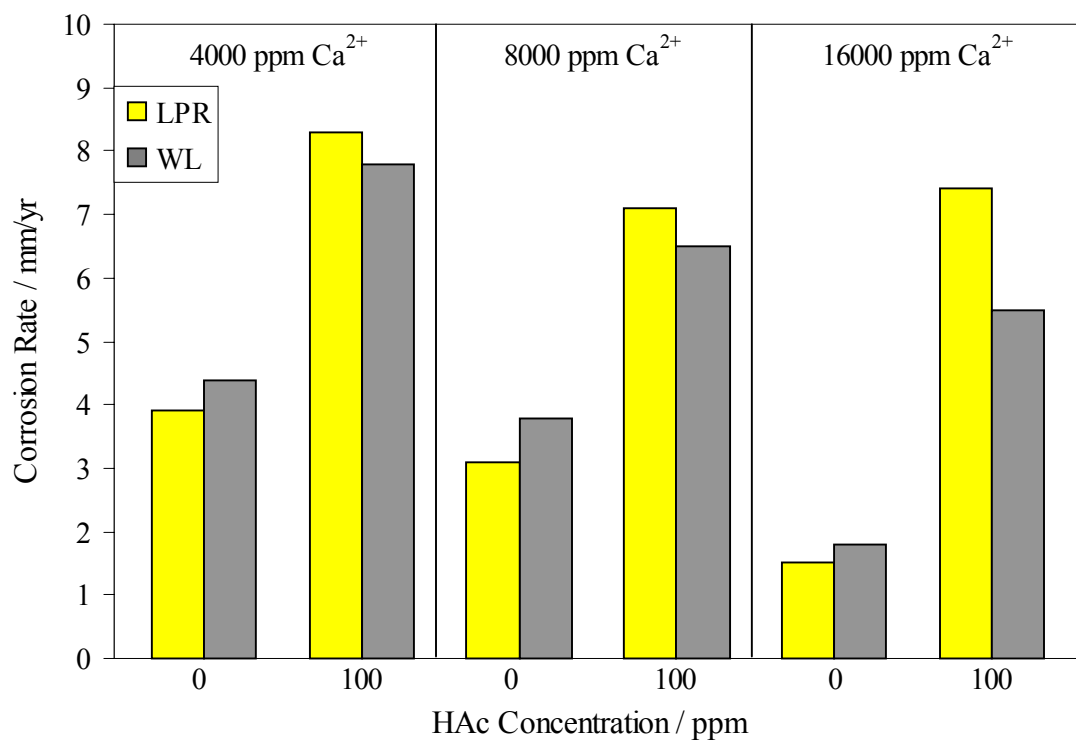


Figure 27. The effect of HAc and Ca²⁺ concentration on the corrosion rate of X-65 steel in bubbling CO₂ solutions (60°C, pH 5, 1000 rpm).

4.10. The Effect of Simulated Brines

Potentiodynamic sweeps were performed in a simulated brine and compared to 3% sodium chloride solutions containing 100 ppm HAc at pH 4, to study the effect of the presence of multiple ions (Ca^{2+} , Mg^{2+} , Sr^{2+} , K^+ , HCO_3^-) on the electrochemical reactions. The potentiodynamic sweeps for the two solutions is shown in Figure 28. It is evident that no difference is apparent for the anodic reaction. There is a change in the cathodic reaction; however, and this is probably due to scaling of the electrode due to the pH increase during the potentiodynamic sweep.

A comparison between the weight loss and LPR measurements was made between solutions containing only 3% sodium chloride and the simulated brine solutions containing 100 ppm HAc at pH 4. The results in Figure 29, show that no significant difference can be seen from the weight loss measurements, measured over twenty-four hours between the two solutions.

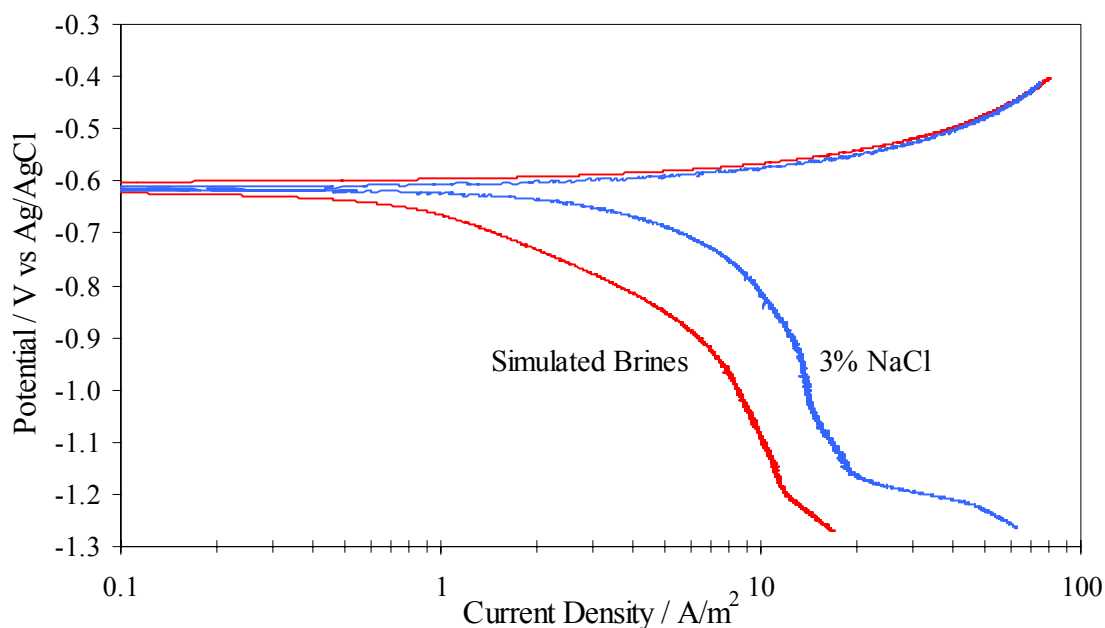


Figure 28. Potentiodynamic sweeps in 3% NaCl and simulated brine solutions containing 100 ppm HAc (22°C, pH 4, 1000 rpm)

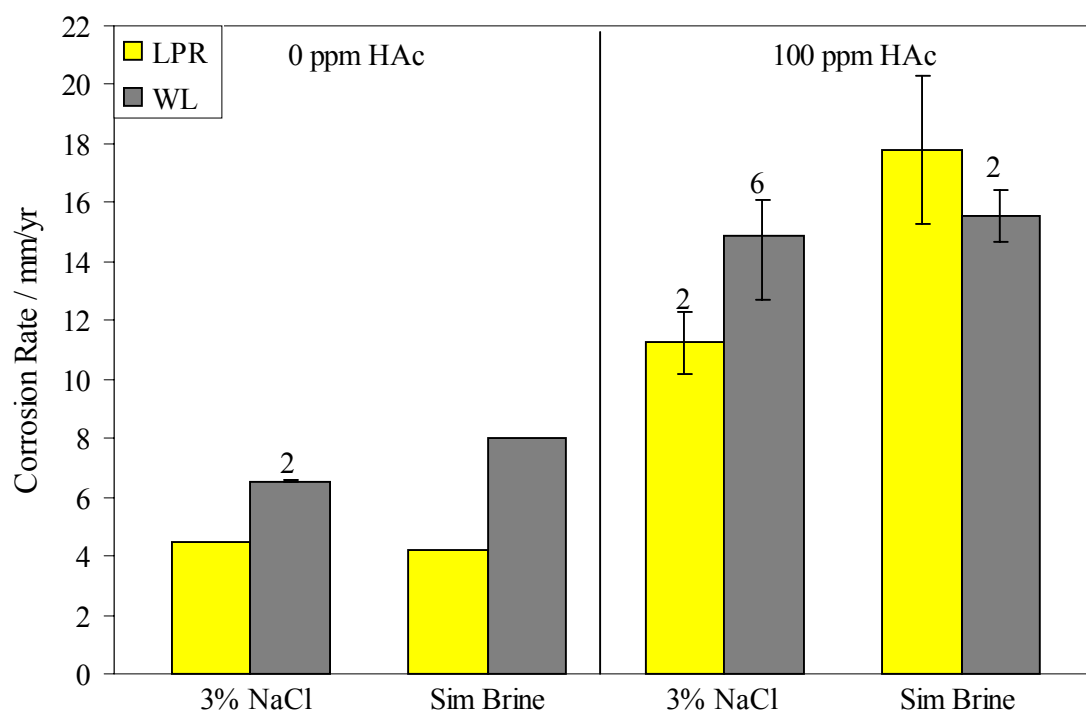


Figure 29. The effect of simulated brines and HAc concentration on the corrosion rate of X-65 steel in bubbling CO₂ solutions (60°C, pH 4, 1000 rpm). Error bars represent the maximum and minimum experimental values.

5. Electrochemical Modeling

In order to model the experimental results, the nature of the measured cathodic and anodic currents must be found. HAC can influence the cathodic reaction in CO₂ corrosion according to at least two possible scenarios. The first is HAC acting as a source of hydrogen ions through dissociation and the second is HAC being directly reduced on the metal surface. The possibility of direct reduction of HAC on the steel surface was not supported by the experimental data. Further, the predicted corrosion rates under this assumption (Chapter 6) were not in agreement with those found experimentally. This adds further weight to the argument that HAC acts solely as a source of hydrogen ions and is not directly reduced on the steel surface.

The experimental evidence seems to suggest that HAC acts solely as a source of hydrogen ions and therefore a slight modification to the hydrogen ion reduction equation, in the calculation of the limiting current, needs to be made. Only one anodic reaction is assumed to be present, which is the dissolution of iron.

5.1. Hydrogen Reduction

To find the effect of charge transfer and mass transfer on hydrogen ion reduction, the cathodic part of the rate equation is used (West 1964)

$$i_{(H^+)} = i_{0(H^+)} \left(\frac{[H^+]_s}{[H^+]_b} \exp\left(\frac{\alpha_c F}{RT} \eta\right) \right) \quad (5.1)$$

where $i_{0(H^+)}$ is the exchange current density in A/m², $[H^+]_s$ and $[H^+]_b$ are the concentrations of hydrogen ions at the metal surface and bulk, respectively in mol/m³, α_c is the symmetry factor, and η is the overpotential from the reversible potential in V. The

overpotential is the difference between the applied potential and the reversible potential.

The reversible potential for hydrogen reduction (E_{rev}) is found from (Nesic 1996)

$$E_{rev(H^+)} = -\frac{2.303RT}{F} pH - \frac{2.303RT}{2F} \log P_{H_2} \quad (5.2)$$

where P_{H_2} is the partial pressure of hydrogen in atm. The partial pressure of hydrogen was assumed to be zero in the experiments. The surface hydrogen ion concentration can be found from the mass transfer equation

$$i_{(H^+)} = k_m F ([H^+]_b - [H^+]_s) \quad (5.3)$$

where k_m is the mass transfer coefficient of hydrogen in m/s. Substitution of Equation 5.3 into 5.1 and solving for $[H^+]_s$ yields the final current density vs voltage equation for H^+ reduction

$$\frac{1}{i_{(H^+)}} = \frac{1}{i_{a(H^+)}} + \frac{1}{i_{lim(H^+)}} \quad (5.4)$$

where $i_{a(H^+)}$ is the activation current density in A/m^2 and $i_{lim(H^+)}$ is the diffusion limiting current density in A/m^2 . The activation current density is given by

$$i_{a(H^+)} = i_{0(H^+)} \times 10^{-\frac{\eta}{b_c}} \quad (5.5)$$

where $i_{0(H^+)}$ is the exchange current density in A/m^2 and b_c is the cathodic Tafel slope in V/dec. The temperature dependence of the cathodic Tafel slope is given by

$$b_c = \frac{2.303RT}{\alpha_c F} \quad (5.6)$$

while the temperature dependence of the exchange current density is given by

$$\frac{i_0}{i_o^{ref}} = e^{-\frac{\Delta H}{R} \left(\frac{1}{T} - \frac{1}{T_{ref}} \right)} \quad (5.7)$$

where ΔH is the enthalpy of activation in kJ/mol and i_o^{ref} is the reference exchange current measured at some reference temperature, T_{ref} . The exchange current density for hydrogen ion reduction was taken as 5×10^{-2} A/m² at 20°C and the enthalpy of activation was taken as 30 kJ/mol (Nesic 1996).

The diffusion limiting current density from Equation 5.4 is calculated by

$$i_{lim(H^+)}^d = k_m F [H^+]_b \quad (5.8)$$

where the mass transfer coefficient is found from the rotating cylinder correlation of Eisenberg (1954)

$$Sh = \frac{k_m d}{D} = 0.0791 \times Re^{0.7} \times Sc^{0.356} \quad (5.9)$$

where d is the diameter of the electrode in m, D is the hydrogen diffusion coefficient in m²/s, Re is the Reynolds number and Sc is the Schmidt number. The temperature dependence of the diffusion coefficient is given by

$$D = D_{ref} \left(\frac{T}{T_{ref}} \right) \left(\frac{\mu_{ref}}{\mu} \right) \quad (5.10)$$

where D_{ref} is the diffusion coefficient at a reference temperature T_{ref} , μ is the viscosity in kg/(ms) and μ_{ref} is the viscosity at a reference temperature. At 20°C, the viscosity of water is 1.002 kg/(m s) (Dugstad 1994) and the diffusion coefficient of the hydrogen ion is 9.31×10^{-9} m²/s (Atkins, 1982). The water density in kg/m³ is found from

$$\rho = 1152.3 - 0.5116T \quad (5.11)$$

while the water viscosity is given by

$$\mu = \mu_{ref} \times 10^{\frac{1.3272(2-t) - 0.001053(20-t)^2}{t+105}} \quad (5.12)$$

5.2. Limiting Current From HAc

Vetter (1976) proposed that limiting currents could result from chemical reactions if a chemical reaction precedes the hydrogen ion reduction reaction. He termed this limiting current a “chemical reaction” limiting current. Vetter then derived equations to predict the chemical reaction limiting currents produced in stagnant weak acid solutions using HAc as the example. Nestic et al. (1995) expanded the equations to flowing systems using carbonic acid as the weak acid. In order to predict the limiting currents in the case of flowing systems in the presence of HAc, Vetter’s derivation will need to be re-derived with flow taken into account.

The reaction preceding the hydrogen ion reduction is the dissociation of HAc.



The rate of reaction for hydrogen ion production is given by

$$v = k_f[\text{HAc}] - k_r[\text{Ac}^-][\text{H}^+] \quad (5.14)$$

where v is the rate of hydrogen production, k_f is the forward reaction rate and k_r is the backward reaction rate. The forward reaction order is assumed to be one, so the rate of reaction does not depend on the concentration of HAc. The rate of reaction for hydrogen ion production is then given by

$$v = v_0 - k_r[\text{Ac}^-][\text{H}^+] \quad (5.15)$$

At equilibrium $v = 0$

$$v_0 = k_r[Ac^-][H^+] = kc_b \quad (5.16)$$

where $k = k_r[Ac^-]$ and c_b is the equilibrium concentration of the hydrogen ion.

Substitution of Equation 5.16 into Equation 5.15 yields

$$v = v_0 \left(1 - \frac{c}{c_b} \right) = v_0(1 - u) \quad (5.17)$$

where u is the nondimensional concentration of hydrogen ions. The chemical reaction current will result from the gradient of hydrogen ions between the diffusion layer and the metal surface. In order to find the concentration profile the steady state mass balance (Fick's second law) for the case of a homogeneous chemical reaction will need to be solved.

$$\frac{\partial c}{\partial t} = \frac{\partial}{\partial x} \left(D \frac{\partial c}{\partial x} \right) + v \quad (5.18)$$

Equation 5.18 is simplified by assuming steady state ($\partial c/\partial t = 0$) and the diffusion coefficient, D , is not a function of temperature. Substitution of Equation 5.17 into Fick's second law yields

$$\frac{\partial^2 u}{\partial x^2} + \frac{(1-u)}{\delta_r^2} = 0 \quad (5.19)$$

In order to solve Equation 5.19, two boundary conditions are needed:

- In the limiting current case, the concentration of hydrogen ions approaches zero at the metal surface so

$$x = 0 \quad u = \frac{c}{c_b} = 0 \quad (5.20)$$

- At the mass transfer boundary layer the concentration of hydrogen ions is equal to the concentration of hydrogen ions in the bulk

$$x = \delta_m \quad u = \frac{c}{c_b} = 1 \quad (5.21)$$

Vetter assumed that the concentration of hydrogen ions is in equilibrium infinitely far from the surface, which is the case for stagnant or laminar flow conditions.

Integration of Equation 5.19, with the two boundary conditions yields

$$u = 1 + \frac{e^{x/\delta_r}}{e^{2\delta_r/\delta_m} - 1} + \frac{e^{-x/\delta_r}}{e^{-2\delta_r/\delta_m} - 1} \quad (5.22)$$

where δ_r and δ_m are the reaction and mass transfer layer thicknesses, respectively, and are calculated from

$$\delta_r = \sqrt{\frac{Dc_b}{v_0}} = \sqrt{\frac{Dc_b}{kc_b}} = \sqrt{\frac{D}{k_r[Ac^-]}} \quad (5.23)$$

$$\delta_m = \frac{D}{k_m} \quad (5.24)$$

where D is the diffusivity of hydrogen ions in m^2/s . The limiting current is found from

$$i_{\lim(H^+)} = FD \left. \frac{\partial c}{\partial x} \right|_{x=0} = FDc_b \left. \frac{\partial u}{\partial x} \right|_{x=0} = \frac{FDc_b}{\delta_r} \left(\frac{1 + e^{-2\delta_m/\delta_r}}{1 - e^{-2\delta_m/\delta_r}} \right) \quad (5.25)$$

A more simplified form is given by

$$i_{\lim(H^+)} = Fc_b \sqrt{Dk_r[Ac^-]} f \quad (5.26)$$

when δ_r is substituted in Equation 5.25 and f is defined as the flow factor which is given by

$$f = \frac{1 + e^{-2\delta_m/\delta_r}}{1 - e^{-2\delta_m/\delta_r}} \quad (5.27)$$

The calculated reaction limiting currents are compared to the experimentally observed limiting currents in solutions de-oxygenated using N₂ or CO₂ in Table 5-1.

Table 5-1. Comparison between calculated reaction limiting currents and the experimental limiting currents. (Note “—“ denotes no data available)

Conc of HAc (ppm)	Experimental i_{lim} in N ₂ (A/m ²)	Experimental i_{lim} in CO ₂ (A/m ²)	Calculated i_{lim} (A/m ²)
0	2	3	2
10	--	4	578
100	6	12	1830
1000	47	57	5780
5000	--	94	12900

It is evident that the calculated reaction limiting currents are not in agreement and are even orders of magnitude larger than the measured values. This is proof that the limiting currents measured in the presence of HAc are not reaction rate controlled. It is worth noting that the flow factor, in the presence of HAc, is equal to unity since the reaction layer thickness is typically two orders in magnitude smaller than the mass transfer boundary layer as the dissociation is very fast (3.2×10^5 1/s).

Since the limiting currents are not reaction limiting, they could be mass transfer limiting. The diffusion limiting current density has the same form as the limiting current density for the hydrogen ion and is given by

$$i_{lim(HAc)}^d = k_m F [HAc]_b \quad (5.28)$$

where k_m is the HAc mass transfer coefficient in m/s and $[\text{HAc}]_b$ is the bulk concentration of HAc.

The calculated reaction limiting currents using Equation 5.28 are compared to the experimentally observed limiting currents in solutions de-oxygenated using N_2 or CO_2 in Table 5-2.

Table 5-2. Comparison between calculated mass-transfer limiting currents and experimental limiting currents. (Note “—“ denotes no data available)

Conc of HAc (ppm)	Experimental i_{lim} in N_2 (A/m^2)	Experimental i_{lim} in CO_2 (A/m^2)	Calculated i_{lim} (A/m^2)
0	2	3	--
10	--	4	1
100	6	12	7
1000	47	57	69
5000	--	94	347

It is evident that the calculated limiting currents are similar in magnitude to the experimental values. In bubbling N_2 solutions, the measured and calculated limiting currents are in agreement. The limiting currents measured in bubbling CO_2 solutions would be in better agreement with the calculated values if the contribution of hydrogen ions and carbonic acid to the limiting currents were taken into account.

If HAc acts as a source of hydrogen only, then it is not involved in a separate cathodic reaction at the metal surface and only increases the limiting current as previously discussed. Therefore, in the limiting current region for hydrogen ion reduction, HAc transport to the metal surface must be accounted for through modification

of the current density vs potential equation of hydrogen. With this in mind, the hydrogen current density versus voltage equation now has the form

$$\frac{1}{i_{(H^+)}} = \frac{1}{i_{a(H^+)}} + \frac{1}{i_{\text{lim}(H^+)}^d + i_{\text{lim}(HAc)}^d} \quad (5.29)$$

where the limiting current density for HAc is given by Equation 5.28.

Since carbonic acid is also a weak acid like HAc, it would be consistent to assume that it too, would only act as a source of hydrogen ions and add to the limiting current.

With this modification, the equation now has the final form of

$$\frac{1}{i_{(H^+)}} = \frac{1}{i_{a(H^+)}} + \frac{1}{i_{\text{lim}(H^+)}^d + i_{\text{lim}(HAc)}^d + i_{\text{lim}(H_2CO_3)}^d} \quad (5.30)$$

where $i_{\text{lim}(H_2CO_3)}^d$ is found through the derivation below.

5.3. Limiting Currents Arising From the Presence of CO₂

A slight modification to the diffusion limiting current must be made to account for the influence of a chemical reaction limiting current when carbonic acid is present. Using the same derivation as used for HAc, the reaction limiting current for carbonic acid is given by (Nesic 1995)

$$i_{\text{lim}(H_2CO_3)}^r = F[CO_2]_b \sqrt{D_{H_2CO_3} K_{\text{hyd}} k_{\text{hyd}}^f} f \quad (5.31)$$

where $[CO_2]_b$ is the bulk concentration of carbon dioxide in mol/m³, K_{hyd} is the equilibrium constant for carbon dioxide hydration in 1/s, k_{hyd}^f is the rate of hydration of carbon dioxide in 1/s and f is the flow multiplier. The overall equilibrium constant was assumed to be equal to 2.58×10^{-3} 1/s. The multiplier f includes the effect of the reaction

diffusion layer on the limiting current. The bulk concentration of carbon dioxide can be found from

$$[CO_2]_b = k_{CO_2}^d \times P_{CO_2} \quad (5.32)$$

where P_{CO_2} is the partial pressure of CO_2 in bar and $k_{CO_2}^d$ is Henry's constant in mol/bar which is given by (Oddo 1982)

$$k_{CO_2}^d = \frac{14.5}{1.00258} \times 10^{-(2.27+5.65 \times 10^{-3} T_f - 8.06 \times 10^{-6} T_f^2 + 0.075 I)} \quad (5.33)$$

where T_f is the system temperature in Fahrenheit and I is the ionic strength. The forward reaction rate, k_{hyd}^f is found from (Comprehensive Chemical Kinetics 1972)

$$k_{hyd}^f = 10^{5.71+0.0526 \times T_c - 2.94 \times 10^{-4} \times T_c^2 + 7.91 \times 10^{-7} \times T_c^3} \quad (5.34)$$

where T_c is the system temperature in °C.

5.4. Water Reduction

Since the concentration of water is very large near the metal surface, no diffusion limiting current exists, so only the charge-transfer process is considered. The reversible potential and Tafel slope for water reduction was assumed to be the same as hydrogen's (Equation 5.2). The exchange current density at 20°C was taken as 3×10^{-5} A/m² and the enthalpy of activation as 30 kJ/mol (Nesic 1996).

5.5. The Anodic Dissolution of Iron

The dissolution of iron around the corrosion potential was assumed to be under activation control and hence pure Tafel behavior was assumed.

$$i_{(Fe)} = i_{0(Fe)} \times 10^{\frac{\eta}{b_a}} \quad (5.35)$$

From the experimental data, the Tafel slope was found to be 80 mV/dec at all concentrations of HAc, but 40 mV/dec was used when HAc was not present in solution. The exchange current density was not found to be affected by the concentration of iron in solution and a value of 1 A/m^2 (Nesic 1996) was used. The reversible potential of X-65 steel was taken to be -0.488 V and the enthalpy of activation as 40 kJ/mol (Nesic 1996).

5.6. Implementation of the Model

Once implemented the model requires as inputs the temperature, pH, HAc concentration, partial pressure of CO_2 , rotating cylinder diameter, and rotational velocity so that the current density for each reaction is calculated. The corrosion potential then is found by solving the equation

$$\sum i_a = \sum i_c \quad (5.36)$$

which also has the form

$$i_{(Fe)} = i_{(H^+)} + i_{(H_2O)} \quad (5.37)$$

Once the corrosion potential is known, a potentiodynamic sweep can be predicted by solving for the difference between the sum of the cathodic reactions from the anodic reactions. The corrosion current or rate is found from the total cathodic current at the corrosion potential.

6. Semi-Empirical Corrosion Modeling

6.1. The de Waard Corrosion Model (1995)

de Waard and Milliams first reported a CO₂ corrosion model for wet gas pipelines in 1975. The model was based on experimental data (weight loss and LPR measurements) taken from glass cells and autoclaves. The model is considered to be a “worst case” model due to its conservative estimate for the corrosion rate. The model, through the years, has been revised (1991, 1993 and 1995) to take into account new parameters important to the corrosion process as experimental data became available. For example, in the 1991 model revision, the effect of higher pressures, protective film formation, high system pH, presence of hydrocarbons and water condensation were taken into account. All of the parameters are accounted for in the model through the use of factors which are multiplied by the “worst case” corrosion rate.

In 1995, the effect of liquid velocity, steel composition and microstructure were included in the model after new experimental data was performed. The “worst case” corrosion rate was found from the following equation

$$\frac{1}{V_{corr}} = \frac{1}{V_r} + \frac{1}{V_m} \quad (6.1)$$

where V_{corr} is the corrosion rate in mm/yr, V_r is the highest possible reaction rate in mm/yr and V_m is the highest possible mass transfer rate of the corrosive species in mm/yr. The charge transfer reaction rate can be written as

$$V_r = A[H_2CO_3]^n e^{\frac{\Delta E}{RT}} \quad (6.2)$$

where A is a constant, n is the reaction order and ΔE is the energy of activation for the reaction. If the carbonic acid concentration is approximated by the concentration of dissolved carbon dioxide, then the equation has the form

$$V_r = A'(pCO_2)^n e^{-\frac{\Delta E}{RT}} \quad (6.3)$$

where A' is a new constant that includes the Henry's equilibrium constant for CO₂ dissolution, which was approximated by an exponential function. de Waard et al. then took logarithms of both sides to obtain

$$\log(V_r) = c_1 + \frac{c_2}{T} + c_3 \log(pCO_2) \quad (6.4)$$

In 1993, de Waard and Lotz separated the corrosion rate calculation into charge transfer and mass transfer components and, in order to find the effect of the system pH on the charge transfer reaction rate, de Waard and Lotz modified the equation to have the form

$$\log(V_r) = c_1 + \frac{c_2}{T} + c_3 \log(pCO_2) + c_4(pH_{actual} - pH_{CO_2}) \quad (6.5)$$

where pH_{actual} is the actual system pH in the presence of cations such as Ca²⁺, Fe²⁺, Mg²⁺, etc., pH_{CO_2} is the pure pH of the system from CO₂ dissolution only and the c's are constants. The pH of the system from CO₂ is found from

$$pH_{CO_2} = 3.71 + 0.00417T - 0.5 \times \log(pCO_2) \quad (6.6)$$

where pCO_2 is the partial pressure of carbon dioxide in bar.

The mass transfer component of the corrosion rate was found from

$$V_m = k_m [CO_2] \quad (6.7)$$

where k_m is found from a Sherwood correlation for straight pipes (Pickett 1974) having the form

$$Sh = \frac{k_m d}{D} = 0.023 Re^{0.8} Sc^{0.3} \quad (6.8)$$

where D is the diffusivity of the corrosive species in m^2/s , d is the pipe diameter in m , Re is the Reynolds number and Sc is the Schmidt number. de Waard et al. then solved for the mass transfer coefficient and combined the temperature dependent terms into a single constant, c_5 .

$$k_m = .023 \left(\frac{p^{0.5} D^{0.5}}{u^{0.5}} \right) \left(\frac{v^{0.8}}{d^{0.2}} \right) = c_5 \left(\frac{v^{0.8}}{d^{0.2}} \right) \quad (6.9)$$

Substitution of Equation 6.9 into Equation 6.7 and adding the Henry's constant for CO_2 dissolution into the constant c_5 yields

$$V_m = c_5 \left(\frac{v^{0.8}}{d^{0.2}} \right) [pCO_2] \quad (6.10)$$

The constant which, until now, includes only temperature dependent terms (density, viscosity, etc.) was then used in conjunction with Equation 6.5 to fit the experimental data.

The two equations after fitting to the experimental data have the form

$$\log(V_r) = 4.84 + \frac{1119}{T} + 0.58 \times \log(pCO_2) - 0.34(pH_{actual} - pH_{CO_2}) \quad (6.11)$$

$$V_m = 2.8 \left(\frac{v^{0.8}}{d^{0.2}} \right) [pCO_2] \quad (6.12)$$

de Waard et al., through multiplying factors, has made modifications to his worst case corrosion rate calculation to account for new phenomena. The only factor needed to

compare with this work is the factor to account for the presence of carbon in the steel. The presence of carbon was only found to influence the charge-transfer reaction rate (V_r) of Equation 6.1. The new charge transfer reaction rate is given by

$$V_r' = V_r F_c \quad (6.13)$$

where F_c is the carbon factor found from

$$F_c = 1 + 4.5 \times C\% \quad (6.14)$$

where $C\%$ is the carbon percentage in the steel. For the mild steel used in these tests, the carbon percentage was 0.15%.

6.2. An Extension of the de Waard Model to Account for the Presence of HAc

As stated previously, a slight modification to the de Waard et al. model (Equation 6.1) is needed to account for the presence of HAc. In the mass transfer term, V_m , only the transport of the corrosive species, carbonic acid, is accounted for in Equation 6.7. Equation 6.8 can be modified to account for the transport of HAc to the metal surface using

$$V_{m(HAc)} = k_m [HAc] \quad (6.15)$$

where $V_{m(HAc)}$ is the mass transfer term for HAc in mm/yr, k_m is the mass transfer rate of HAc and $[HAc]$ is the bulk concentration of HAc. The mass transfer rate of HAc can be found using Equation 6.8 with an appropriate expression for the diffusivity for HAc (Equation 5.10) when D_{ref} equals $1.24 \times 10^{-9} \text{ m}^2/\text{s}$ at 25°C (Perry 1984). The de Waard et al. model now has the form

$$\frac{1}{V_{corr}} = \frac{1}{V_r} + \frac{1}{V_{m(H_2CO_3)} + V_{m(HAc)}} \quad (6.16)$$

where $V_{m(H_2CO_3)}$ is the mass transfer rate of carbonic acid found from Equation 6.12. The constants in Equations 6.11 and 6.12, which were used to fit the original experimental data have not been changed with the modification to account for HAc.

7. Comparison Between the Electrochemical Model and Experimental Data

7.1. Anodic Reaction

In order to account for the retardation of the anodic reaction with increasing concentrations of HAc, a factor, which is less than one, has been applied to the anodic reaction in the model. The factor was set to unity when the HAc concentration was zero and found to follow a power law with HAc concentration.

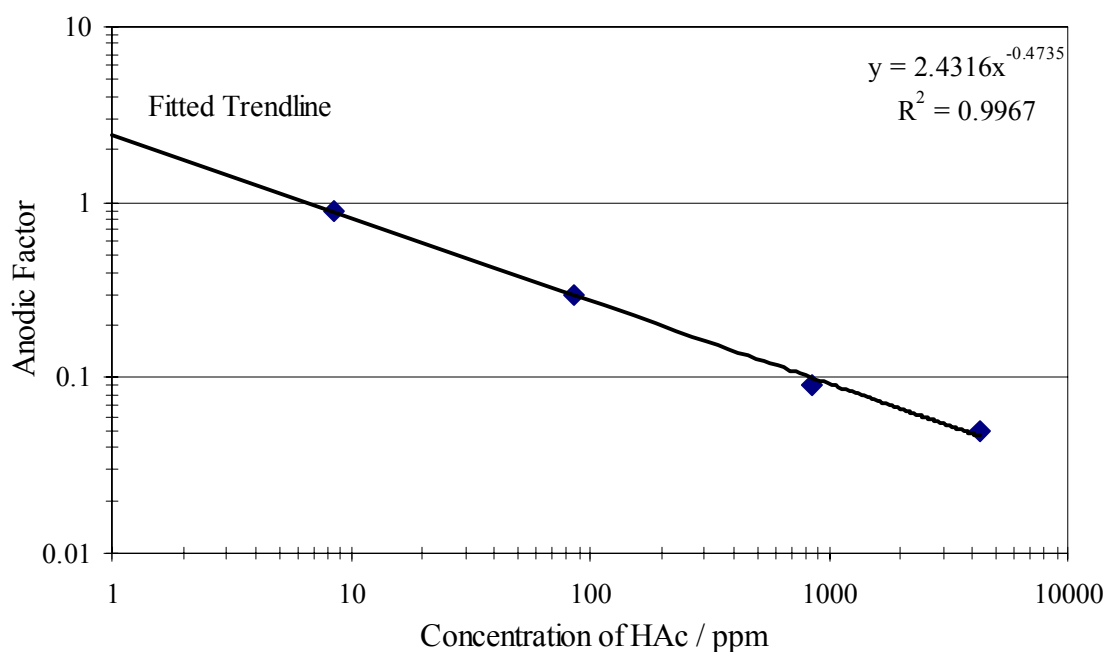


Figure 30. Anodic factor and fitted trend line as a function of HAc concentration.

All of the electrochemical model results shown in the subsequent sections will include the factor found from the equation below

$$f_{anodic} = 2.43[HAc]^{-0.4735} \quad (7.1)$$

where [HAc] is the bulk concentration of HAc in ppm. It is worth noting that the anodic factor will only be applied at room temperature since no evidence is available to suggest its use at higher temperatures.

7.2. The Effect of HAc In Solutions De-Oxygenated Using CO₂

A predicted potentiodynamic sweep, which has been broken into the three individual sources of hydrogen ions, (transport of hydrogen ions from the bulk, and transport and dissociation of both carbonic acid and HAc) to show the effect of HAc is shown in Figure 31. It is clear that under these conditions HAc is the major source of hydrogen ions. Also shown in Figure 31 is the sum of the cathodic currents (total cathodic) and anodic currents (total anodic). This figure will serve as a guide for the comparison of the model and the experimental results.

The comparison between the electrochemical model and the experimental results for solutions de-oxygenated using CO₂ are shown in Figures 32-36. It is evident that the model is in good agreement with the experimental data at all concentrations of HAc studied. The model predicts both the charge transfer and limiting current regions of the cathodic potentiodynamic sweeps very well. The anodic reaction is also predicted very well until passivation of the metal surface occurs at higher overpotentials.

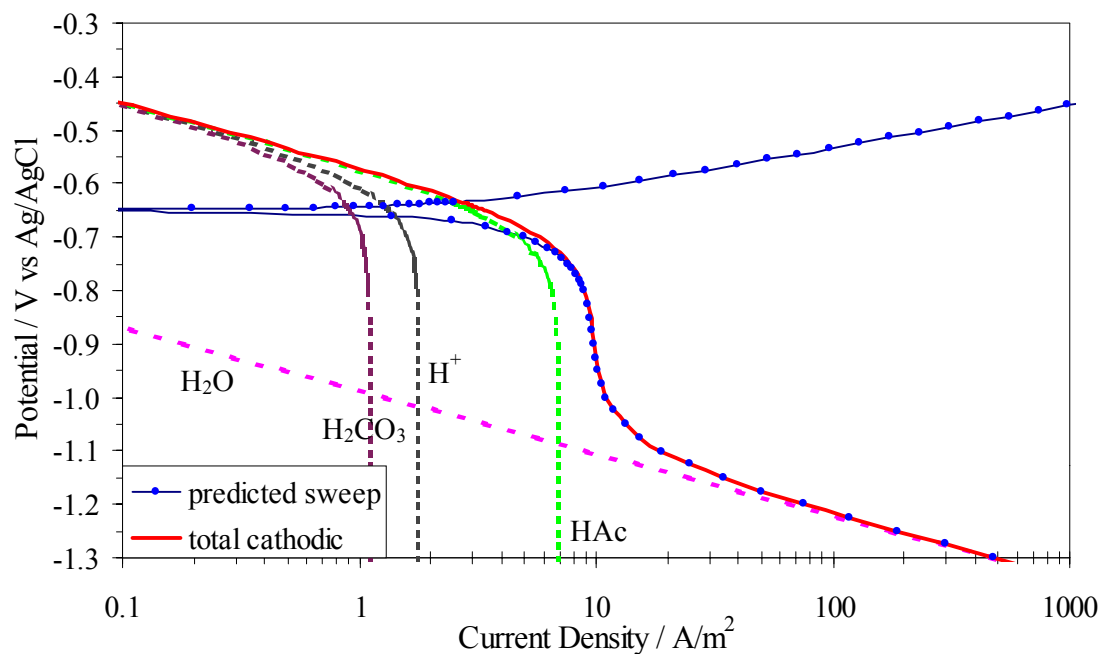


Figure 31. The electrochemical reactions in bubbling CO_2 solutions containing 100 ppm HAc (22°C, pH 4, 1000 rpm).

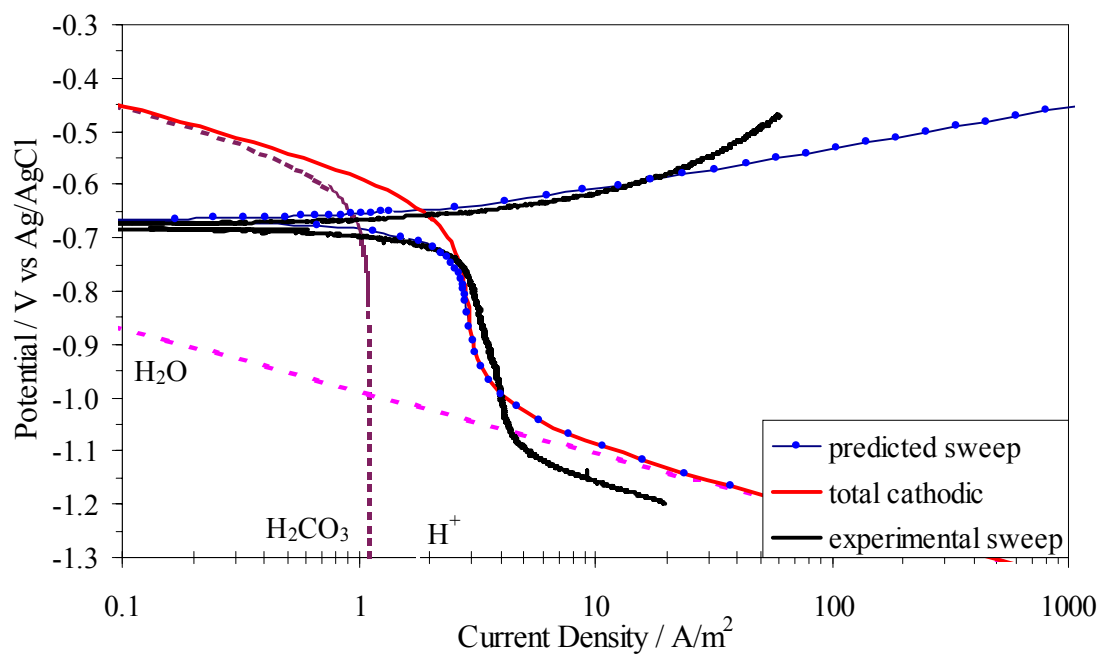


Figure 32. Comparison between the electrochemical model and experimental data in bubbling CO_2 solutions containing 0 ppm HAc (22°C, pH 4, 1000 rpm).

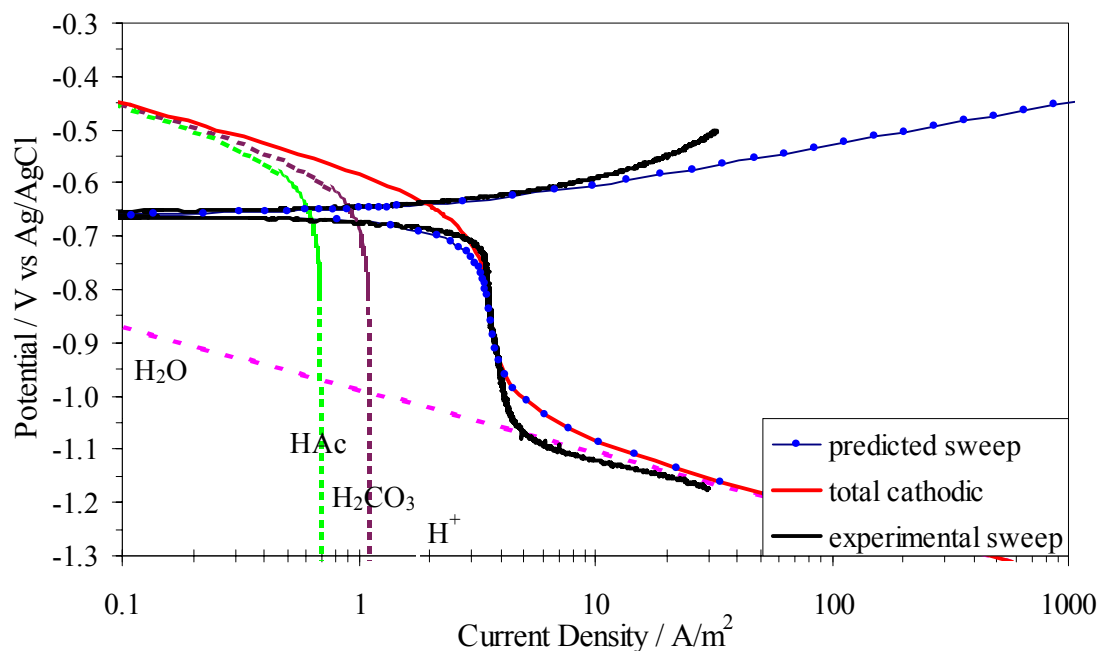


Figure 33. Comparison between the electrochemical model and experimental data in bubbling CO₂ solutions containing 10 ppm HAc (22°C, pH 4, 1000 rpm).

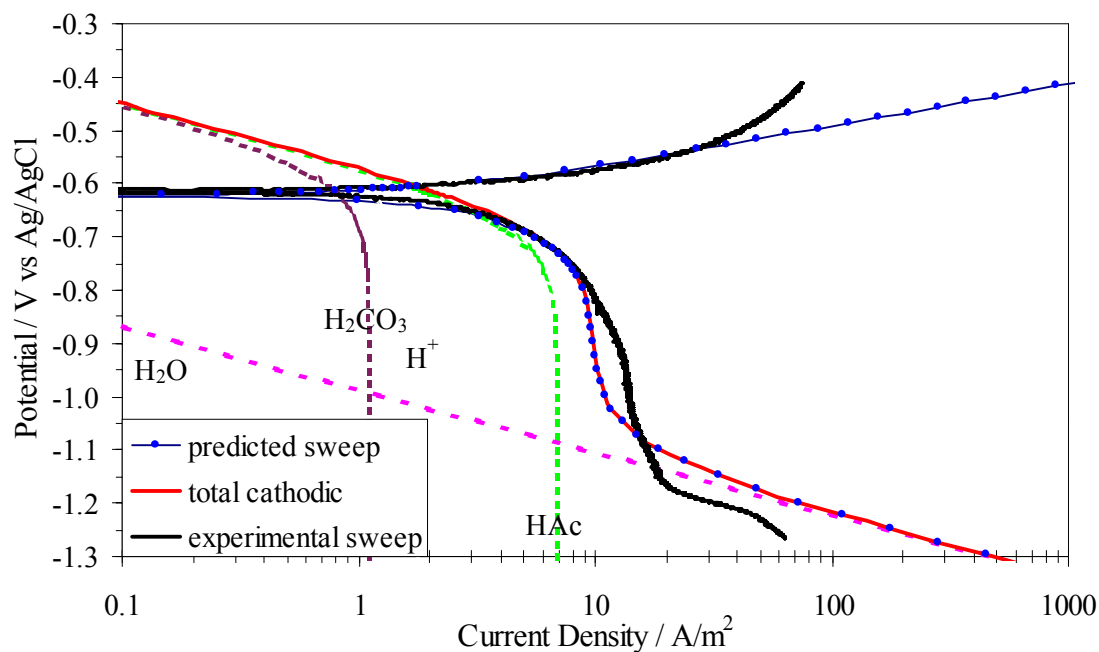


Figure 34. Comparison between the electrochemical model and experimental data in bubbling CO₂ solutions containing 100 ppm HAc (22°C, pH 4, 1000 rpm).

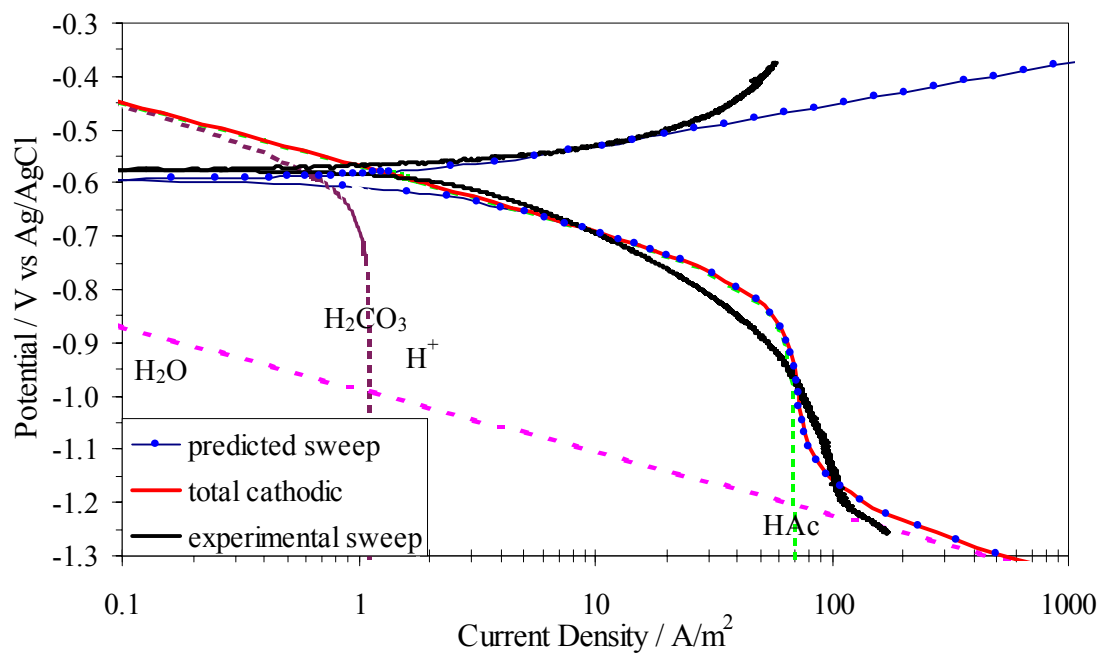


Figure 35. Comparison between the electrochemical model and experimental data in bubbling CO₂ solutions containing 1000 ppm HAc (22°C, pH 4, 1000 rpm).

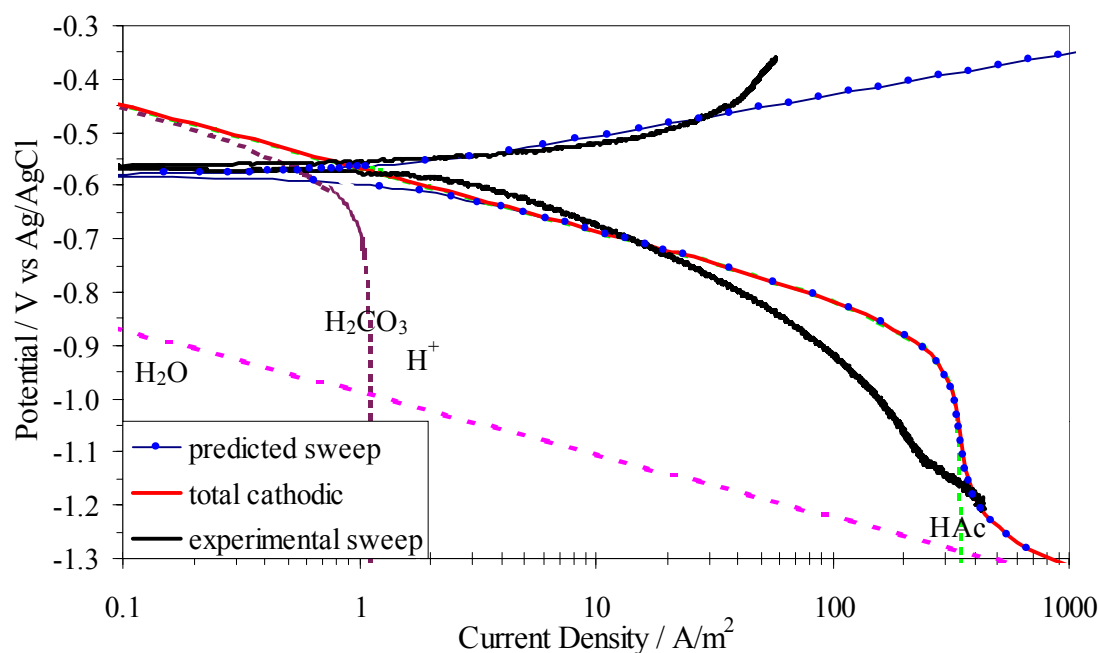


Figure 36. Comparison between the electrochemical model and experimental data in bubbling CO₂ solutions containing 5000 ppm HAc (22°C, pH 4, 1000 rpm).

7.3. The Effect of HAc In Solutions De-Oxygenated Using N₂

The comparison between the electrochemical model and the experimental results de-oxygenated using N₂ are shown in Figures 37-39. The agreement between the model and the experimental results is especially good when no HAc is present (Figure 37). When HAc is present, however, the agreement between the electrochemical model and the experimental results is not as good, which could suggest that the experimental results are in error. The error is not great since the experimental and predicted corrosion potentials are in agreement and, in the case of the 100 ppm HAc potentiodynamic sweep, the limiting current is in agree with the experimental data.

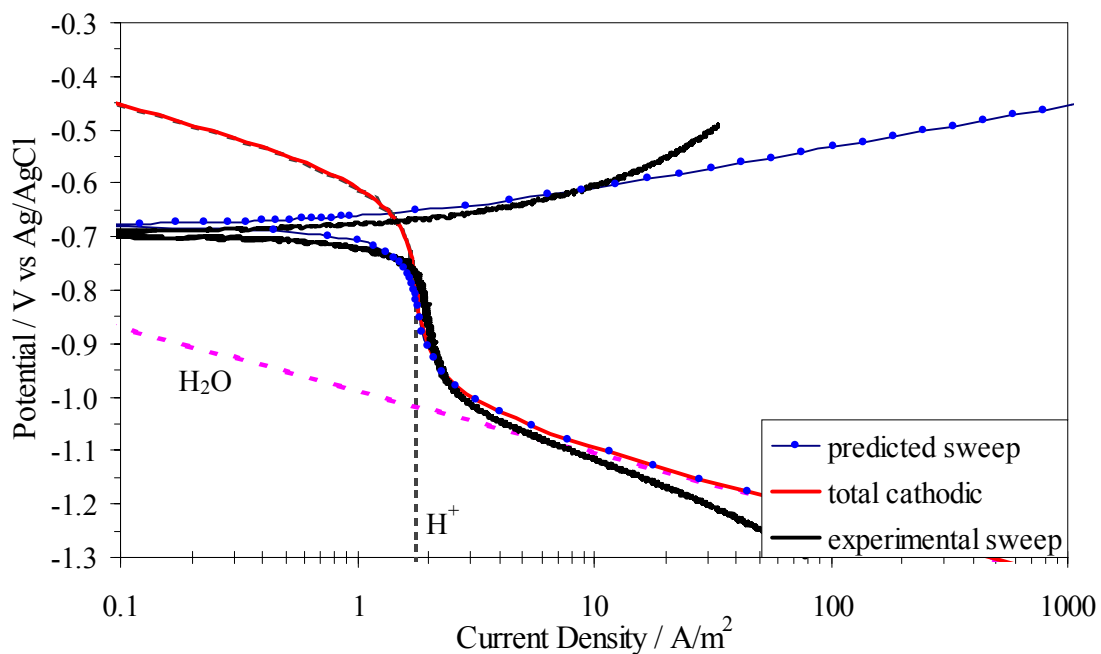


Figure 37. Comparison between the electrochemical model and experimental data in bubbling N₂ solutions containing 0 ppm HAc (22°C, pH 4, 1000 rpm).

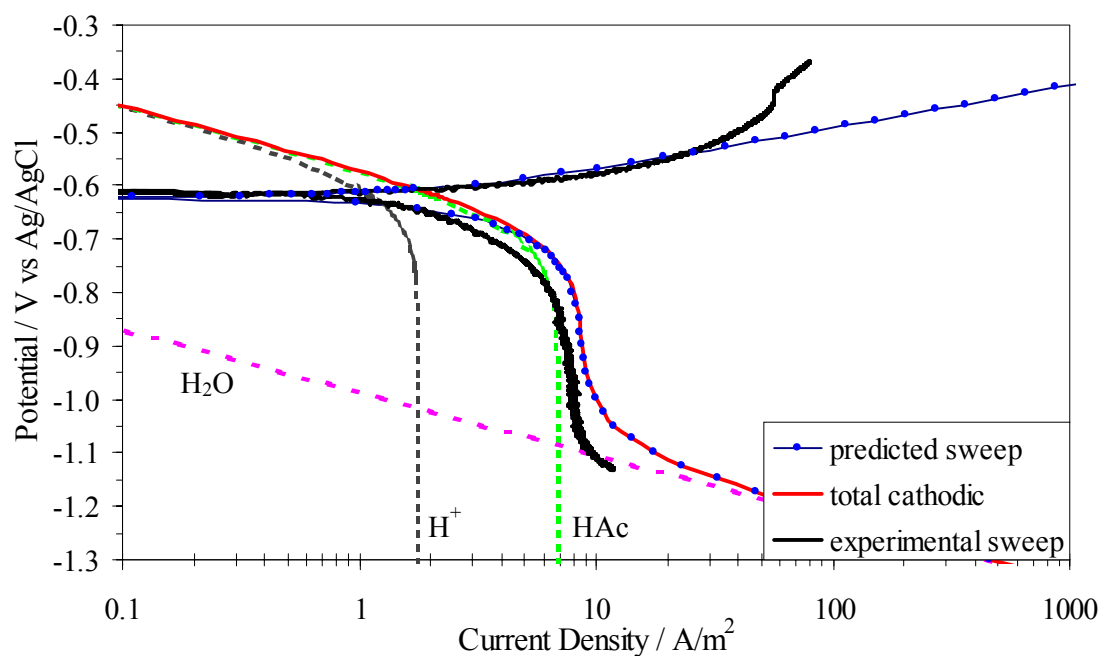


Figure 38. Comparison between the electrochemical model and experimental data in bubbling N₂ solutions containing 100 ppm HAc (22°C, pH 4, 1000 rpm).

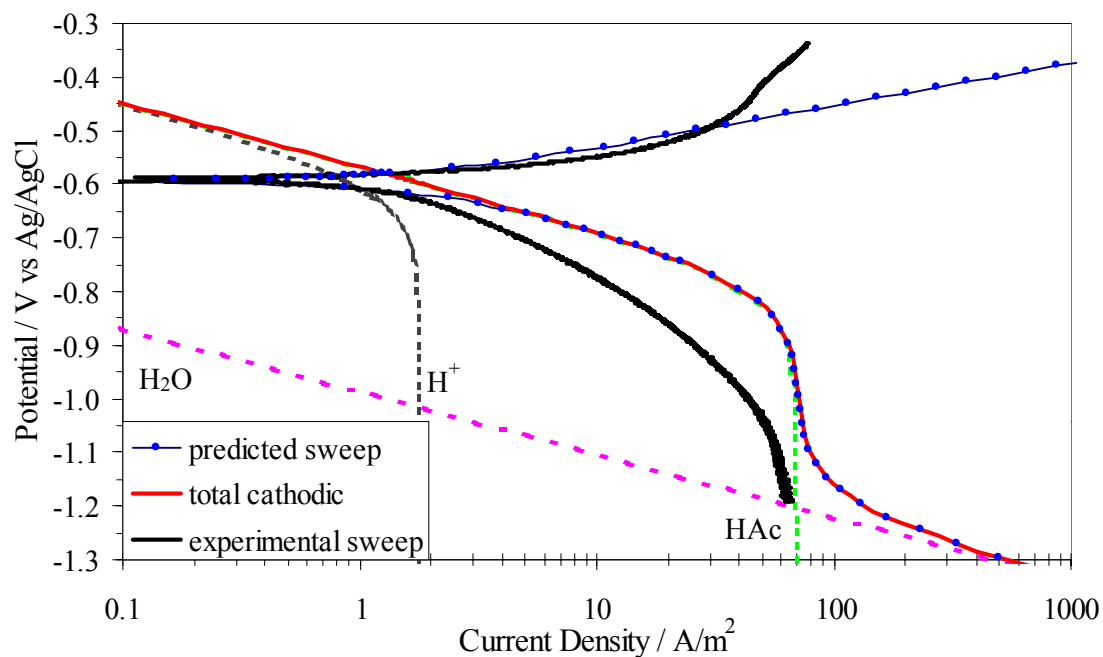


Figure 39. Comparison between the electrochemical model and experimental data in bubbling N₂ solutions containing 1000 ppm HAc (22°C, pH 4, 1000 rpm).

7.4. The Effect of Rotational Velocity

The effect of rotational velocity manifests itself through increased transport of species and particularly HAC to the metal surface. The experimental and predicted potentiodynamic sweeps were found to be in very good agreement at all velocities and are shown in Figure 40-43.

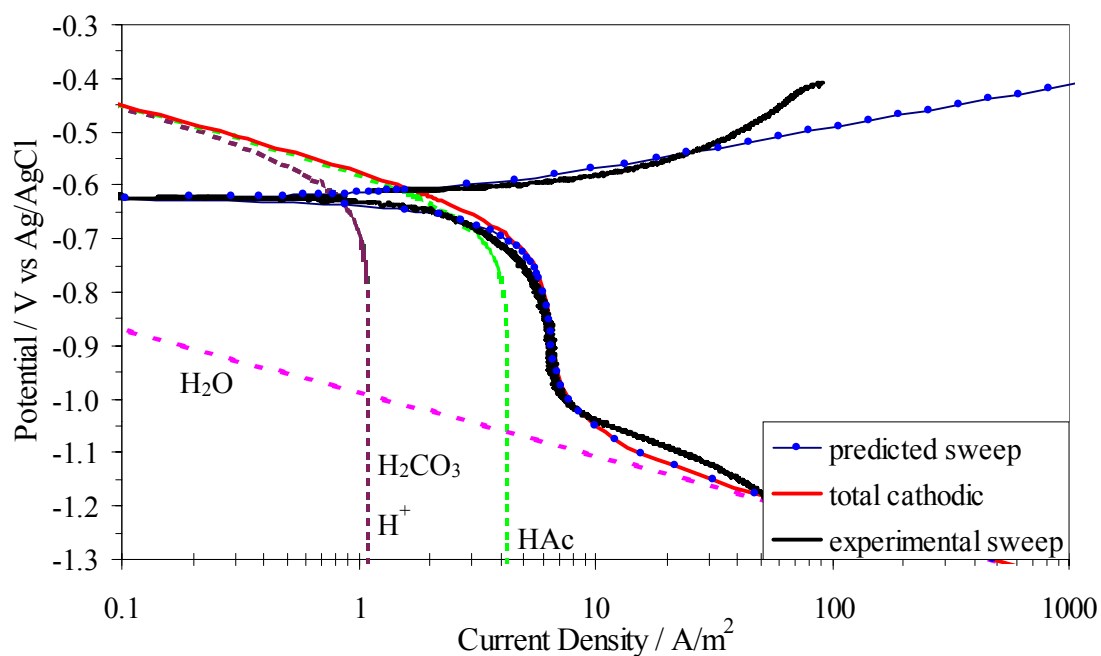


Figure 40. Comparison between the electrochemical model and experimental data in bubbling CO₂ solutions at 500 rpm (22°C, 100 ppm HAC, pH 4).

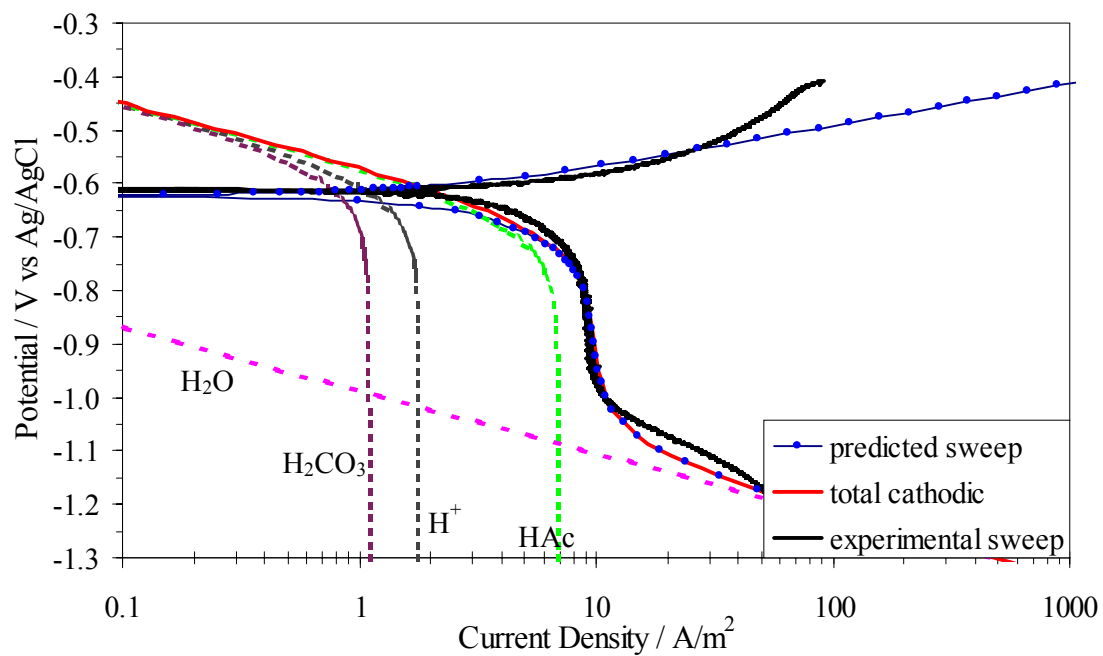


Figure 41. Comparison between the electrochemical model and experimental data in bubbling CO₂ solutions at 1000 rpm (22°C, 100 ppm HAc, pH 4).

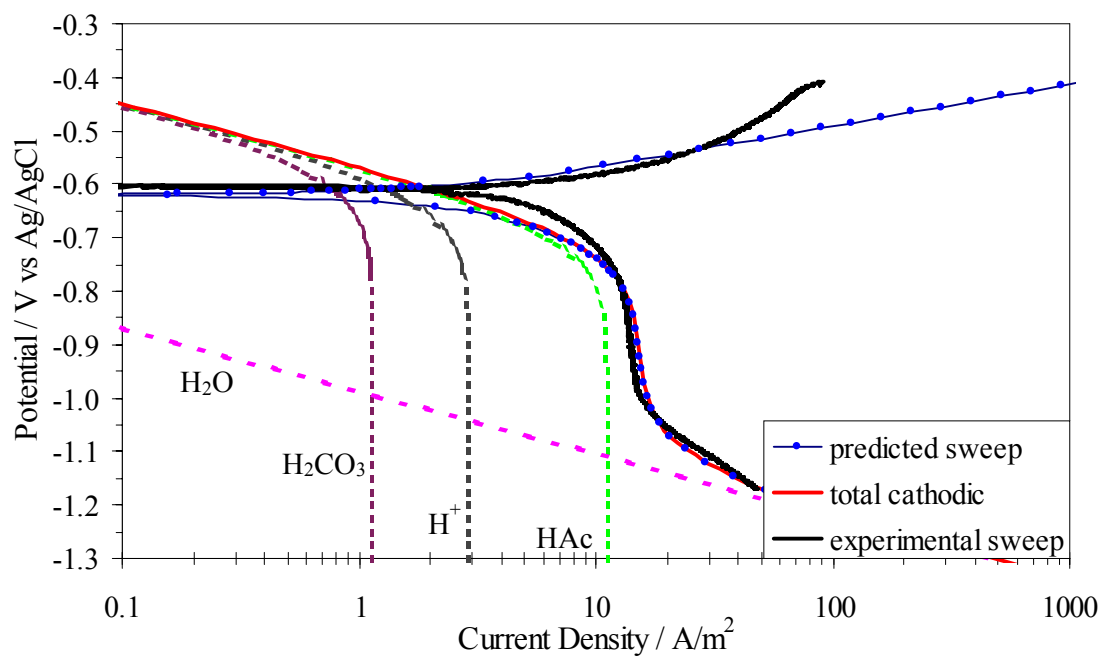


Figure 42. Comparison between the electrochemical model and experimental data in bubbling CO₂ solutions at 2000 rpm (22°C, 100 ppm HAc, pH 4).

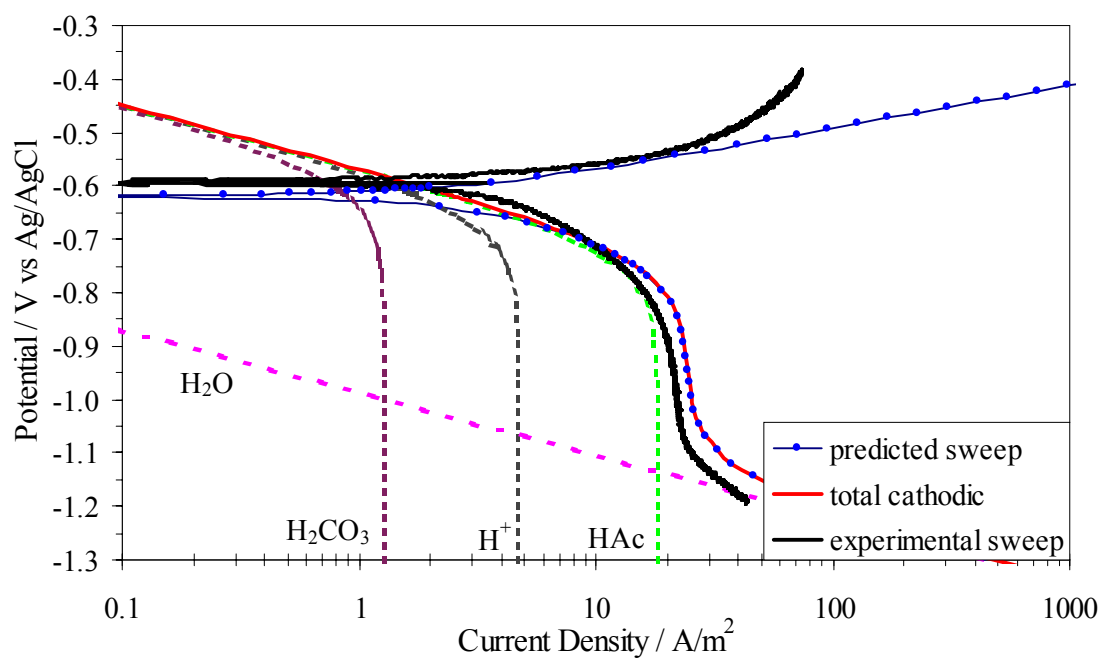


Figure 43. Comparison between the electrochemical model and experimental data in bubbling CO₂ solutions at 4000 rpm (22°C, 100 ppm HAc, pH 4).

7.5. The Effect of pH

The effect of pH is shown in Figures 44-46. The predicted potentiodynamic sweep at pH 4 is shown in Figure 44 and is in good agreement with the experimental data. Since the experimental potentiodynamic sweeps performed at pH 5 and 6 were performed in the presence of HAc, an anodic factor cannot be applied since a baseline (0 ppm) potentiodynamic sweep was not measured at those pHs. Therefore, it is unknown if the anodic factor is accelerated or retarded when compared to the 0 ppm anodic potentiodynamic sweep at pH 5 or 6. The uncorrected predicted potentiodynamic sweeps at pH 5 and 6 are compared to the experimental sweeps in Figures 44 and 45. The predicted corrosion potential is close to the experimental values, which suggests the anodic reaction is only slightly retarded. For the experiment at pH 5 (Figure 45) the predicted limiting current is in agreement with the experimental data but the predicted water reduction line is not. At pH 6 (Figure 46) the agreement between the model and the experimental values would be much better if the predicted water line was shifted to higher potentials to match the experimental water reduction line.

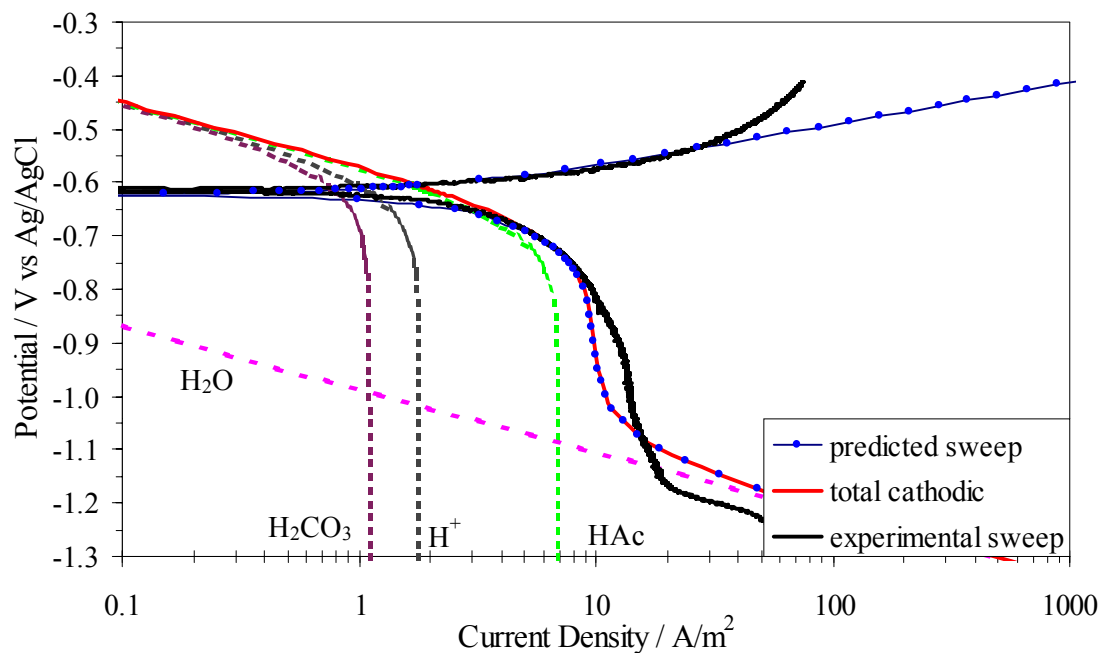


Figure 44. Comparison between the electrochemical model and experimental data in bubbling CO₂ solutions at pH 4 (22°C, 100 ppm HAc, 1000 rpm).

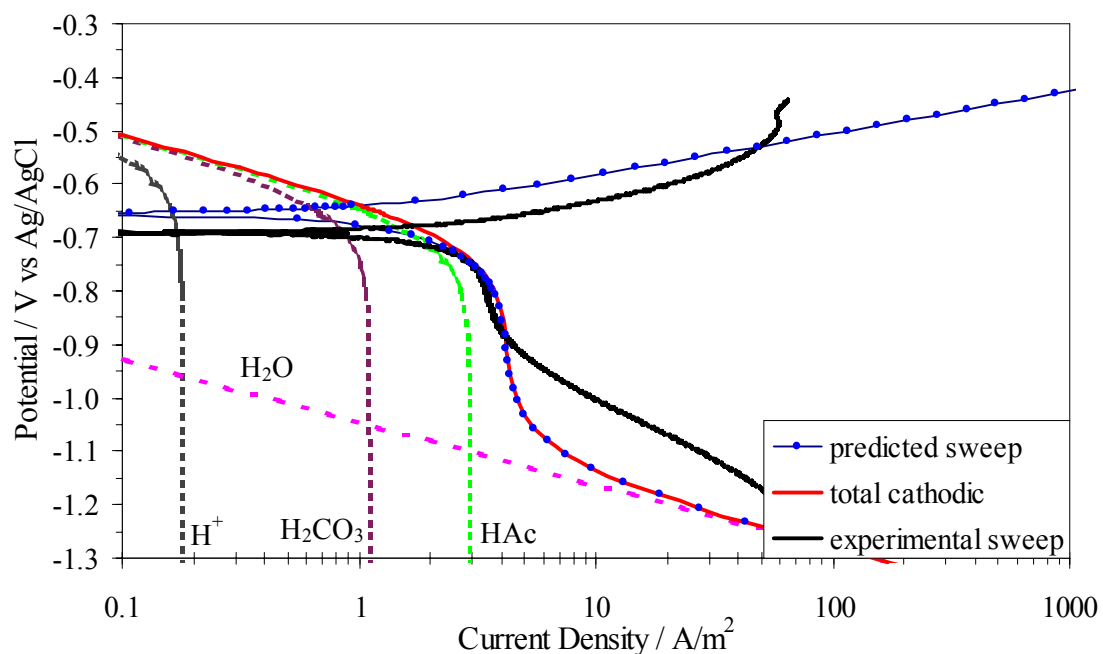


Figure 45. Comparison between the electrochemical model and experimental data in bubbling CO₂ solutions at pH 5 (22°C, 100 ppm HAc, 1000 rpm).

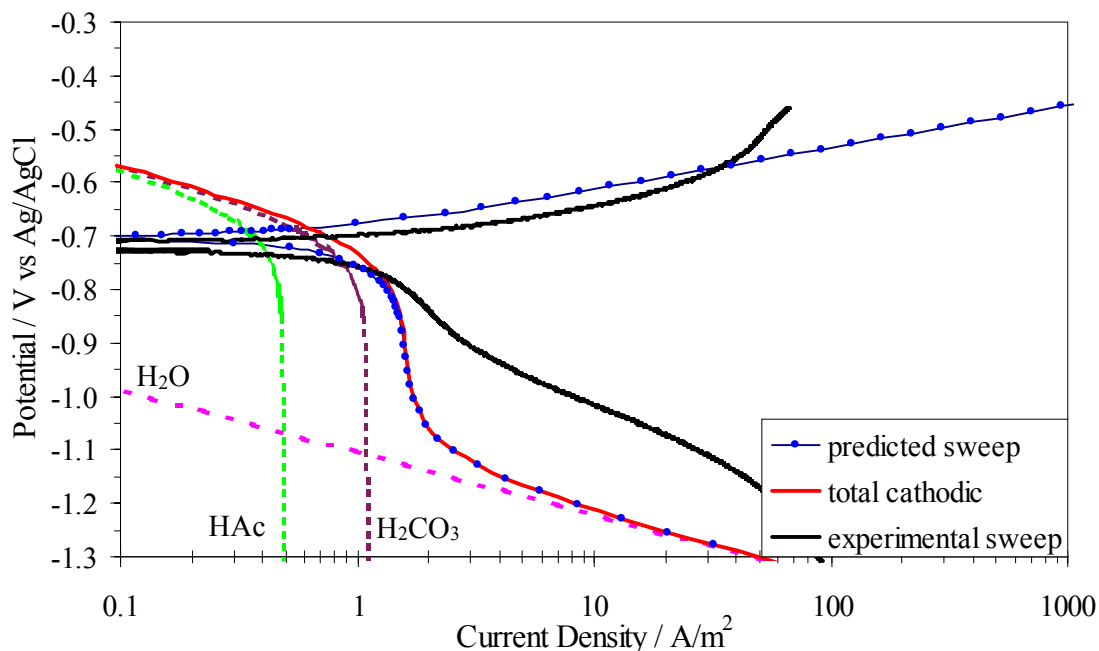


Figure 46. Comparison between the electrochemical model and experimental data in bubbling CO₂ solutions at pH 6 (22°C, 100 ppm HAc, 1000 rpm).

7.6. The Effect of Temperature

The effect of temperature is shown in Figures 47-49. The predicted potentiodynamic sweep at 22°C is shown in Figure 47 and is in good agreement with the experimental data. Again, since the experimental sweeps were performed in the presence of HAc, an anodic factor cannot be applied since a baseline (0 ppm) potentiodynamic sweep was not measured at higher temperatures. It is currently not known if the presence of HAc retards the anodic reaction at temperatures above 22°C. It is worth noting that the experimental and predicted are in good agreement with the exception of the predicted corrosion potential. If an anodic factor were applied to the anodic reaction in the model the corrosion potential would be shifted to more noble values and the experimental and predicted potentiodynamic sweeps would be in better agreement.

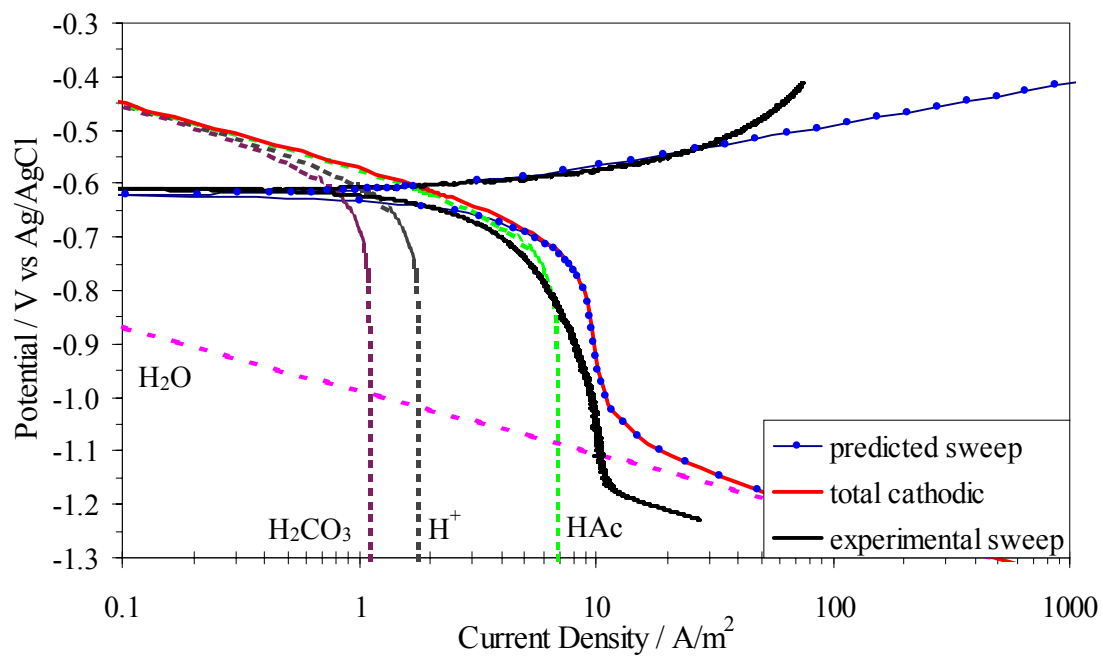


Figure 47. Comparison between the electrochemical model and experimental data in bubbling CO₂ solutions at 22°C (100 ppm HAc, pH 4, 1000 rpm).

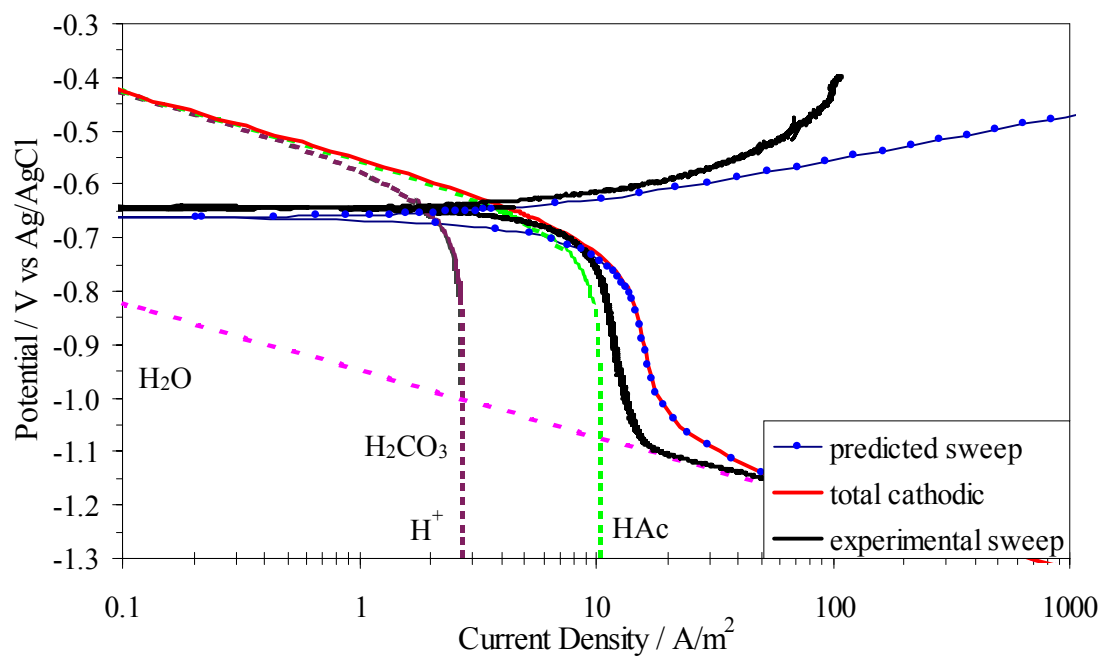


Figure 48. Comparison between the electrochemical model and experimental data in bubbling CO₂ solutions at 40°C (100 ppm HAc, pH 4, 1000 rpm).

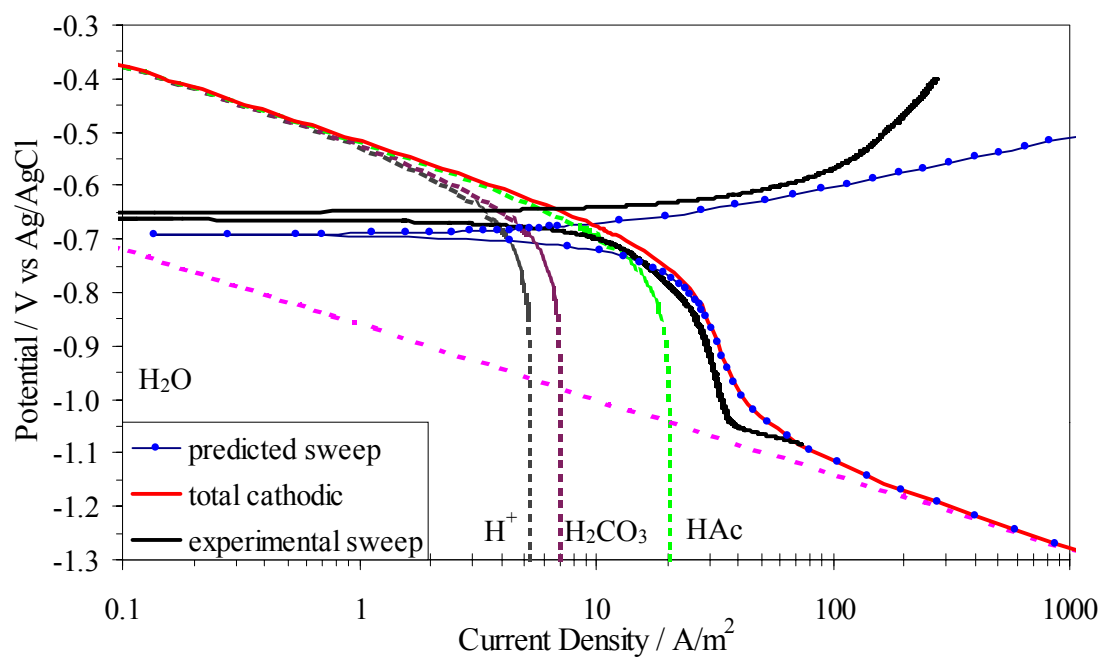


Figure 49. Comparison between the electrochemical model and experimental data in bubbling CO₂ solutions at 80°C (100 ppm HAc, pH 4, 1000 rpm).

8. Comparison Between the Models and Experimental Data

The electrochemical and the modified de Waard model (or GDN model) will be compared to the experimental weight loss data and LPR presented in Chapter 4. In order to compare the modified de Waard model, which is typically used in pipelines, with the experimental data obtained in a RCE, equivalence between the two flow geometries must be found. This equivalence can be achieved using the basis of equal mass transfer coefficients between the two systems. The mass transfer coefficient of hydrogen in a RCE was calculated from the Eisenberg (1954) correlation (Equation 1.11). For pipe flow, the Berger and Hau (1977) correlation is appropriate.

$$Sh_p = \frac{k_m d_p}{D} = 0.0165 \times Re_p^{0.86} \times Sc^{0.33} \quad (7.1)$$

If the RCE mass transfer coefficient of hydrogen is calculated from the Eisenberg correlation, it is then used in the Berger and Hau correlation to solve for the flow velocity in the Reynolds number term. A pipe diameter must also be assumed and was taken as 0.1 m in this work.

The comparison between the LPR, WL and the electrochemical and GDN models at 22°C is shown in Figure 50. At low concentrations of HAc (up to 100 ppm), the agreement between the experimental data and the electrochemical model is very good. Above 100 ppm, the electrochemical model does not agree with the experimental data. This is due, in part, through the use of the anodic factor, which retards the anodic reaction to predict the corrosion potential in the electrochemical model. While retarding the anodic reaction, the corrosion rate is also lowered significantly at high concentrations of

HAc. It is evident that the GDN model grossly over predicts the corrosion rate at all concentrations of HAc.

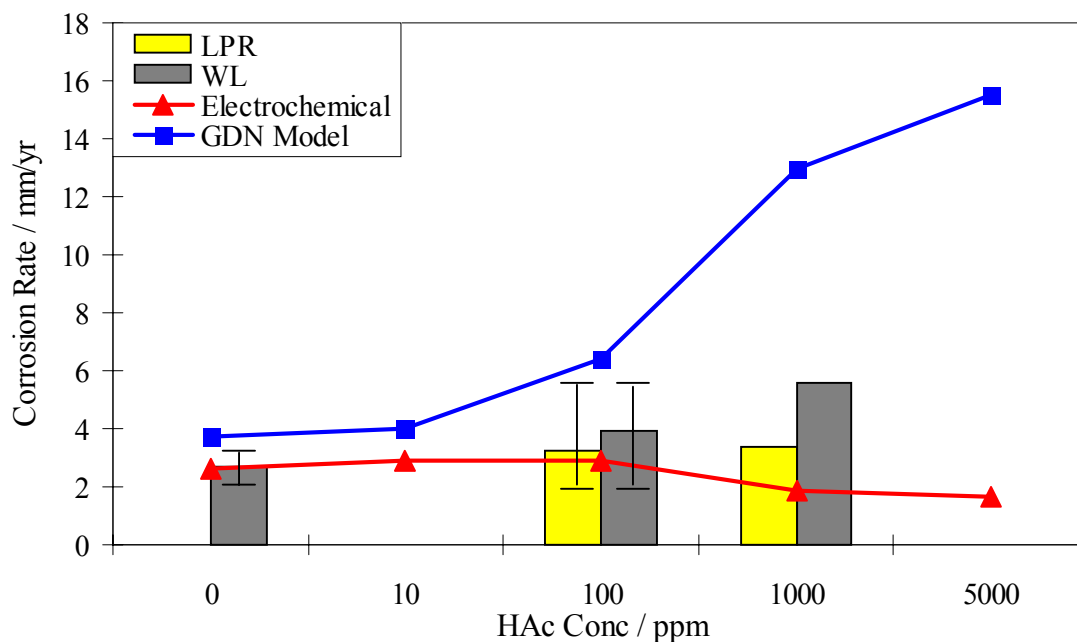


Figure 50. Comparison between the experimental data and electrochemical and GDN models at 22°C (0-5000 ppm HAc, pH 4, 1000 rpm).

The comparison between the LPR, WL, the electrochemical and GDN models at 40°C is shown in Figure 51. It should be noted that the y-axis (corrosion rate scale) has different values than those shown in Figure 50. Both the electrochemical and GDN models are in good agreement with the WL data at low concentrations of HAc. As the HAc concentration is increased, the two models diverge in their predicted values. However, the GDN model is in better agreement with the experimental data throughout the concentrations studied.

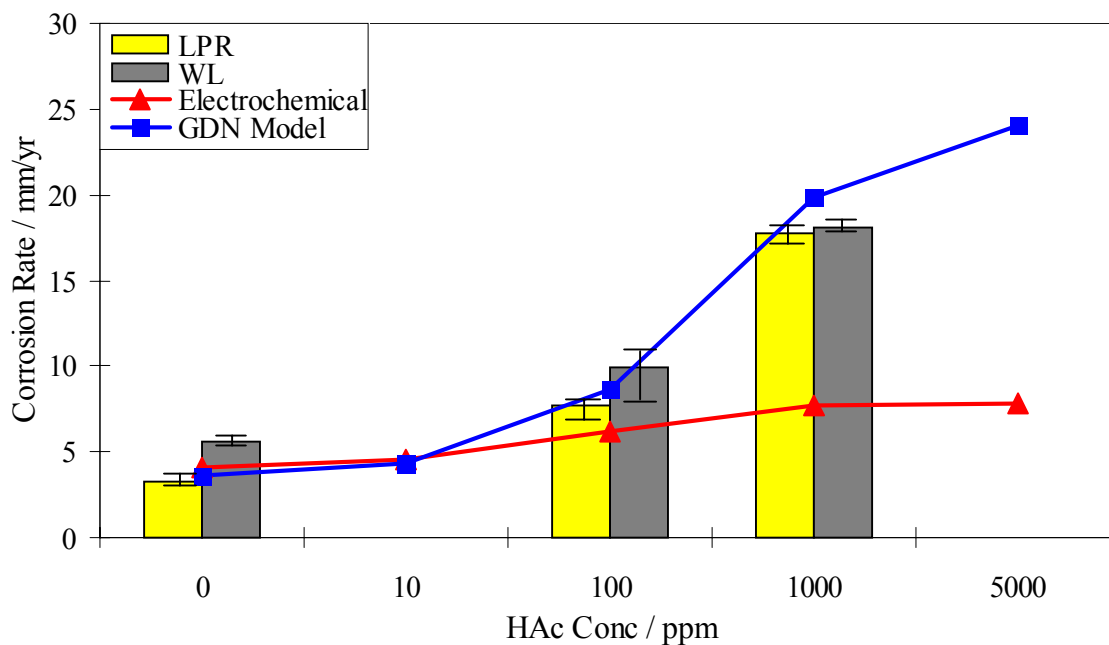


Figure 51. Comparison between the experimental data and electrochemical and GDN models at 40°C (0-5000 ppm HAc, pH 4, 1000 rpm).

The comparison between the LPR, WL, the electrochemical model and GDN models 60°C is shown in Figure 52. It should be noted, again, that the y-axis (corrosion rate scale) has different values than those shown in Figure 51. At low concentrations of HAc (<100 ppm), the electrochemical model is in better agreement with the experimental data than the GDN model. Unfortunately neither model is conservative enough and both under-predict the corrosion rate. At concentrations of 100 ppm and above, the GDN model is in better agreement with the experimental data than the electrochemical model.

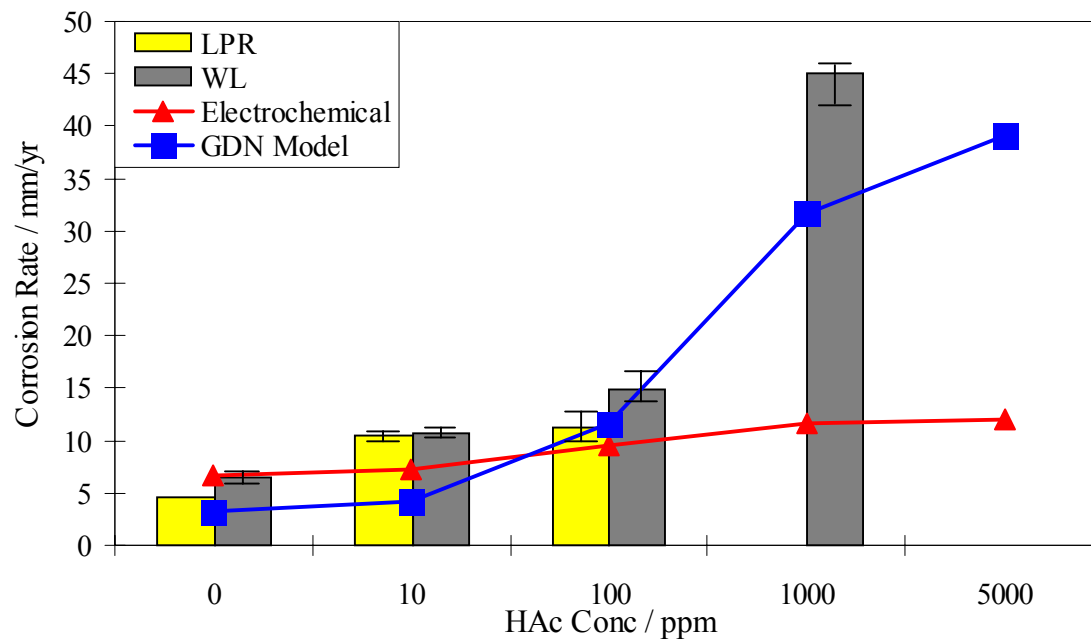


Figure 52. Comparison between the experimental data and electrochemical and GDN models at 60°C (0-5000 ppm HAc, pH 4, 1000 rpm).

9. Conclusions and Future Work

9.1. Conclusions

From the experimental potentiodynamic sweeps, it has been shown that

- the corrosion rate of carbon steel in the presence of HAc is not significantly affected by the presence of HAc since the corrosion rate is dominated by charge transfer control at 22°C.
- HAc did not affect the charge transfer mechanism of the cathodic reaction, but did strongly affect the limiting current.
- the anodic reaction (iron dissolution) was retarded with increasing HAc concentration at 22°C, but the mechanism remained the same.
- the influence of HAc on the corrosion rate of mild steel is more pronounced with increasing temperature.

From the modeling of the experimental data, it has been shown

- that the limiting currents in the presence of HAc are not limited by reaction kinetics, but rather, mass-transfer.
- the predicted and experimental potentiodynamic sweeps agree well when HAc is assumed to be only a source of hydrogen ions at 22°C.
- the de Waard model, with a slight modification, can be used to predict the corrosion rates of mild steel at higher temperatures when HAc is present.

9.2. Future Work

The basic effect of low HAc on the cathodic and anodic reactions has been found at 22°C. Additional work needs to be performed to determine why the potentiodynamic sweeps cannot predict the corrosion rates measured using weight loss or by LPR. Throughout the experimental series, there seemed to be an activation time for the corrosion process, which was not consistent between experiments. It is possible for the anodic reaction to be initially retarded in the presence of HAc but accelerated after significant exposure. If the potentiodynamic sweeps can predict the high corrosion rates then the electrochemical model can be tuned to the potentiodynamic sweeps, and hopefully provide better agreement between the experimental and predicted corrosion rates can be obtained.

Pitting corrosion has also been found under some of the experimental conditions. This phenomenon was unexpected and it would be useful to define under what conditions HAc causes pitting of mild steel. An attempt should be made to define the mechanism of pitting initiation when HAc is present.

All of the experimental work presented here has been performed on film-free surfaces. There have been reports (Hedges 1998, Crolet 1998) of thinner corrosion product films forming in the presence of HAc. It is unknown if the thinner films were the result of a lower system pH or from an interaction of the iron carbonate films and HAc. Also, the characteristics of the iron carbonate films formed (thickness, morphology, porosity, etc.) in the presence of HAc are not known and should be studied.

10. References

1. P.W. Atkins, Physical Chemistry, 2nd Edition, Oxford, England, Oxford University Press, 1985, p F-37.
2. F.P. Berger, K. F.F-L Hau, *Int J Heat Mass Transfer*, Vol 20, 1977, p 1185.
3. J. O'M Bokris, A.K.N. Reddy, Modern Electrochemistry, New York, Plenum Press, 1973.
4. Comprehensive Chemical Kinetics, Vol 6, Amsterdam, The Netherlands, Elsevier Publishing Company, 1972.
5. J-L. Crolet, N. Thevenot, and A. Dugstad, "Role of Free Acetic Acid on the CO₂ Corrosion of Steels," CORROSION/1999, Paper No. 24, (Houston, TX: NACE International, 1999).
6. C. de Waard, D.E. Milliams, "Carbonic Acid Corrosion of Steel", *Corrosion*, Vol 31, No 5, 1975, p 175.
7. C. de Waard, U. Lotz, and D.E. Milliams, "Prediction Model for CO₂ Corrosion Engineering in Wet Gas Pipelines", *Corrosion*, Vol 47, No 12, 1991, p 976.
8. C. de Waard, U. Lotz, "Prediction of CO₂ Corrosion in Carbon Steel", CORROSION/1993, Paper No. 69, (Houston, TX: NACE International 1993).
9. C. de Waard, U. Lotz, A. Dugstad, "Influence of Liquid Flow Velocity on CO₂ Corrosion: A Semi-Empirical Model", CORROSION/1995, Paper No. 128, (Houston, TX: NACE International, 1995).
10. A. Dugstad, L. Lunde, K. Videm, "Parametric Study of CO₂ Corrosion of Carbon Steel," CORROSION/1994, Paper No. 14, (Houston, TX: NACE International, 1994).
11. M. Eisenberg, C.W. Tobias, C.R. Wilke, *J Electrochemical Society*, Vol 101, 1954, p 306.
12. D.R. Gabe, G.D. Wilcox, J. Gonzalez-Garcia, F.C. Walsh, "The Rotating Cylinder Electrode: Its Continued Development and Application", *J Applied Electrochemistry*, Vol 28, No 49, 1998, p 759.
13. Y. Garsany, D. Pletcher, B. Hedges, "The Role of Acetate in CO₂ Corrosion of Carbon Steel: Has the Chemistry Been Forgotten?" CORROSION/2002, Paper No. 2273, (Denver, CO: NACE International, 2002).

14. Y.M. Gunaltun, D. Larrey, "Correlation of Cases of Top of Line Corrosion With Calculated Water Condensation Rates", CORROSION/2000, Paper No. 71, (Houston, TX: NACE International 2000).
15. B. Hedges, L. McVeigh, "The Role of Acetate in CO₂ Corrosion: The Double Whammy" CORROSION/1999, Paper no. 21, (Houston TX: NACE International 1999).
16. M.W. Joosten, J. Kolts, J.W. Hembree, M. Achour, "Organic Acid Corrosion in Oil and Gas Production," CORROSION/2002, Paper No. 2294, (Denver, CO: NACE International, 2002).
17. G. Liu, D.A. Tree, M.S. High, "Relationships Between Rotating Disk Corrosion Measurement and Corrosion in Pipe Flow," *Corrosion Science*, Vol 50, No 8, August 1994, p 584.
18. D. MacDonald, M.C.H. McKubre, J.O.M. Bockris, B.E. Conway, R.E. White, Modern Aspects of Electrochemistry, New York, Plenum Press, Vol 14, 1982, p 61.
19. E. McCafferty, *J Corrosion Science and Engineering*. Vol 39, 1997, p 243.
20. S. Netic, G.T. Solvi, J. Enerhaug, "Comparison of the Rotating Cylinder and Pipe Flow Tests for Flow-Sensitive Carbon Dioxide Corrosion," *Corrosion*, Vol 51, No. 10, 1995, p 773.
21. S. Netic, J. Postlethwaite, S. Olsen, "An Electrochemical Model for Prediction Of Corrosion of Mild Steel in Aqueous Carbon Dioxide Solutions," *Corrosion Science*, Vol 52, No 4, April 1996, p 280.
22. S. Netic, B.F.M. Pots, J. Postlethwaite, N. Thevenot, "Superposition of Diffusion and Chemical Reaction Controlled Limiting Currents – Application to CO₂ Corrosion," *J Corrosion Science and Engineering*, Vol 1, Paper 3, 1995.
23. S. Netic, Magnus Novdsveen, Rolf Nyborg, Aage Stangeland, , "A Mechanistic Model for CO₂ Corrosion with Protective Iron Carbonate Films," CORROSION/2001, Paper No. 1040, (Houston TX: NACE International 2001).
24. J.E.Oddo, M.B. Tomsom, "Simplified Calculation of CaCO₃ Saturation at High Temperature and Pressures in Brine Solutions," SPE of AIME, 1982, p 1583.
25. R.H. Perry, D. Green, Perry's Chemical Engineers' Handbook, 50th ed, McGraw-Hill, 1984.
26. Pickett, *Electrochimica Acta*, Vol 19, 1974, p 875.

27. K.J. Vetter, Electrochemical Kinetics – Theoretical and Experimental Aspects, New York, Academic Press, 1976.
28. J.M. West, Electrodeposition and Corrosion Processes, Van Nostrand, 1964, p 36